

Experimental Measurements of X-ray Scattering from Technical Aluminum Accelerator Vacuum Chamber Surfaces, and Comparison with an Analytical Model

G. Dugan and K. Sonnad

CLASSE, Cornell University, Ithaca, NY, US

T. Ishibashi

KEK, Tsukuba, Japan

I. INTRODUCTION

Synchrotron radiation X-rays generated by particle beams within the vacuum chamber of particle accelerators generally scatter from the chamber walls multiple times before they are ultimately absorbed. The distribution of photon absorption sites, as well as the photon energy spectrum, is an important input into the computation of such quantities as the distribution and energy of primary photoelectrons which seed the electron cloud, and the distribution of heat loads on the chamber wall. While it is possible to precisely calculate the pattern of synchrotron radiation generated by the beam, the locations of the ultimate sites at which the radiation is absorbed depend also on the details of the scattering process, as well as the geometry and composition of the vacuum chamber.

Recently, as part of the CESR-TA program [1], a new tracking program called **Synrad3D** [2, 3], which includes both the generation and scattering of synchrotron radiation photons in accelerator vacuum chambers, has been developed to address this issue. **Synrad3D** treats both specular and diffuse scattering from the vacuum chamber surface, and can incorporate the detailed three-dimensional geometry of the walls. The specular reflectivity of the surface material is taken from an LBNL database [4]. The diffuse scattering from a rough surface is based on an analytical model [5, 6]. To validate the accuracy of the scattering model used in **Synrad3D**, it is important to compare its predictions directly with actual X-ray scattering data from rough surfaces, typical of accelerator vacuum chambers. That comparison is the purpose of this paper.

To make the comparison, well-characterized X-rays beams from BESSY II were used to measure the scattering from samples of aluminum technical vacuum chamber surfaces from CESR. The data includes both relative measurements of the shape of the angular distributions of scattered X-rays, and absolute measurements of the reflectivity. Comparisons of the data for both types of measurements with the **Synrad3D** scattering model will be made.

II. SCATTERING MODEL

The relative reflected power per unit solid angle is the sum of the specularly reflected fraction and the diffusely reflected fraction, multiplied by the smooth-surface reflectivity:

$$\frac{1}{P_0} \frac{dP_{\text{tot}}}{d\Omega} = R(y, \lambda) \left(P_{\text{spec}}(y, \lambda) \frac{dF_{\text{spec}}}{d\Omega} + (1 - P_{\text{spec}}(y, \lambda)) \frac{dF_{\text{diff}}}{d\Omega} \right). \quad (1)$$

In this expression, P_0 is the incident power, $R(y, \lambda)$ is the smooth-surface reflectivity, $y = \cos \psi_i$ is the cosine of the incident polar angle relative to the surface normal, and λ is the photon wavelength. The differential solid angle is $d\Omega = dx d\phi$, where $x = \cos \psi_r$ is the cosine of the reflected polar angle, and ϕ is the reflected angle out of the plane of incidence.

The smooth-surface reflectivity $R(y, \lambda)$ characterizes the probability of reflection when a photon strikes a perfectly smooth surface. This reflectivity is a function of the incident angle, the photon energy, and the material properties of the surface. The smooth-surface reflectivity used for comparisons with the data in this paper is illustrated in Fig. 1. The reflectivity is plotted as a function of photon energy, for different values of the incident grazing angle $\theta_i = \pi/2 - \psi_i$. It has been taken from an LBNL X-ray scattering database [4]. The particular surface layer (a 5 nm carbon monoxide film) has been chosen because, as discussed below, the absorption edges of both carbon and oxygen (as well as aluminum) are observed in the reflectivity measurements presented here.

A technical vacuum chamber surface is not perfectly smooth. For a rough surface, $P_{\text{spec}}(y, \lambda)$ is the probability of specular reflection of a photon. This probability depends on the rms surface roughness σ , the photon wavelength λ , and the cosine of the incident polar angle, y . An explicit formula for this probability is [5]

$$P_{\text{spec}}(y, \lambda) = e^{-\frac{16\pi^2\sigma^2y^2}{\lambda^2}}. \quad (2)$$

For the technical vacuum chamber surfaces studied in this paper, the rms surface roughness $\sigma \sim 100$ nm is much greater than the X-ray wavelength, for all except the lowest energy photons. In this regime, except at very small grazing angles, diffuse scattering from the surface dominates over specular reflection. This is illustrated in Fig. 2, in which the probability of specular reflection is plotted vs. photon energy for various incident grazing angles.

A. Specular reflection

For a perfectly smooth surface, all scattering is specular and in the plane of incidence. The differential fraction of specularly reflected radiation power is given by

$$\frac{dF_{\text{spec}}}{d\Omega} = \delta(x - y)\delta(\phi).$$

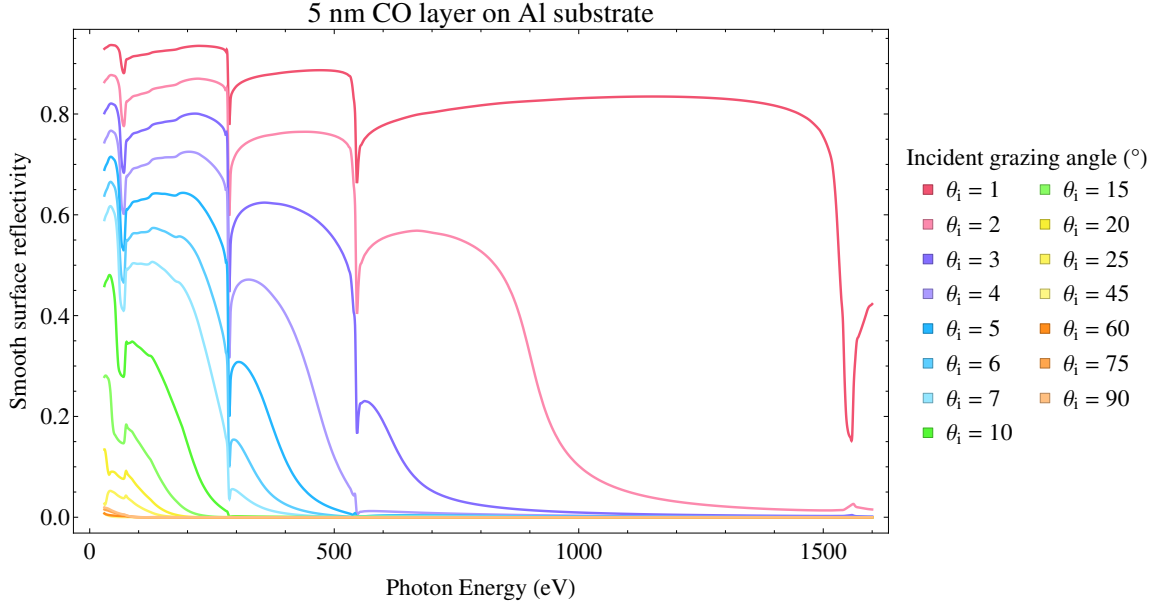


FIG. 1. Smooth surface reflectivity for a 5 nm CO film on an Al substrate: from [4]

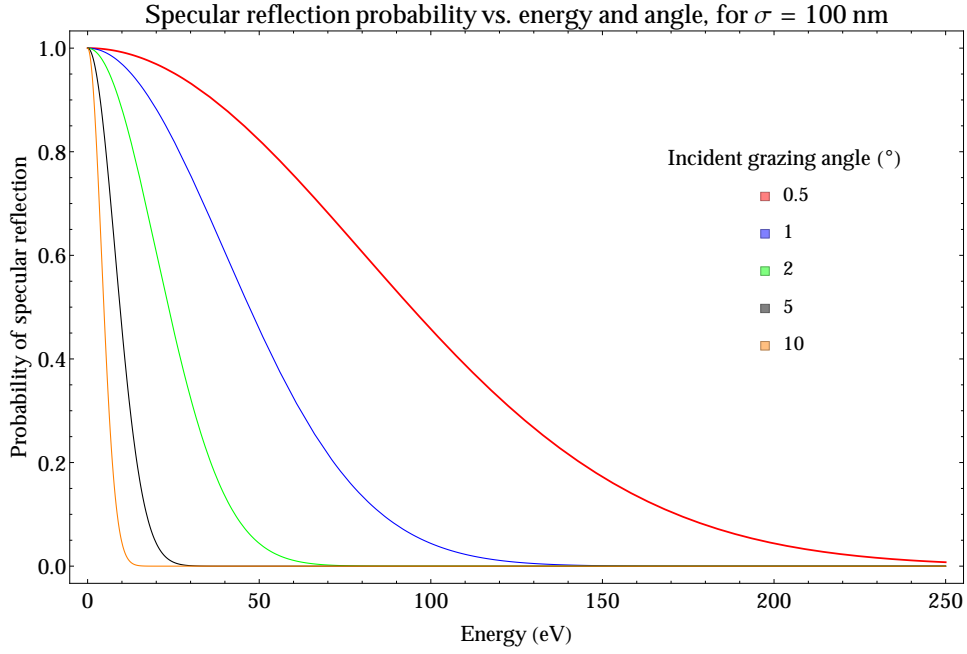


FIG. 2. Specular reflection probability [5], vs. photon energy and angle, for an rms surface roughness of 100 nm. The curves have been computed from Eq. 2.

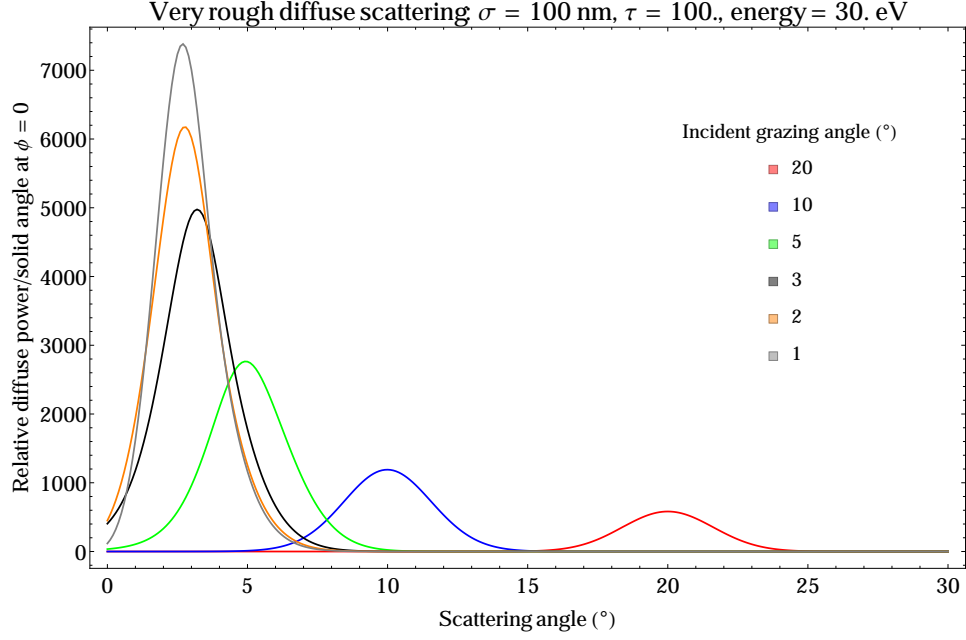


FIG. 3. Diffuse scattering reflected grazing angle distributions for 30 eV photons. The full diffuse scattering expression (Eq. 4) has been used to calculate these curves.

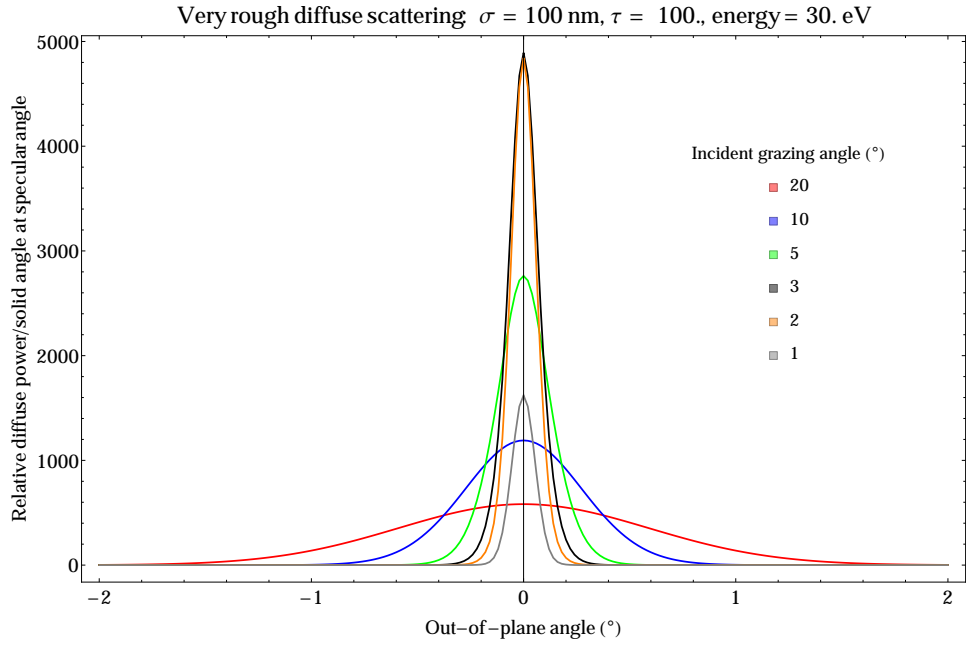


FIG. 4. Diffuse scattering out-of-plane reflected angle distributions for 30 eV photons. The full diffuse scattering expression (Eq. 4) has been used to calculate these curves.

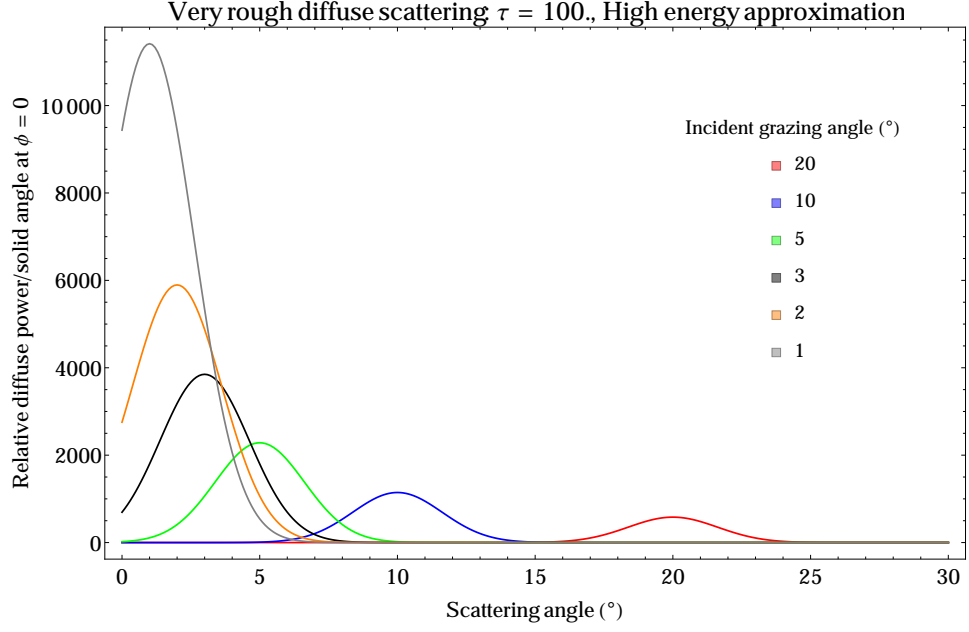


FIG. 5. Diffuse scattering reflected grazing angle distributions for high energy photons. The curves are calculated from the approximate relation given in Eq. 15.

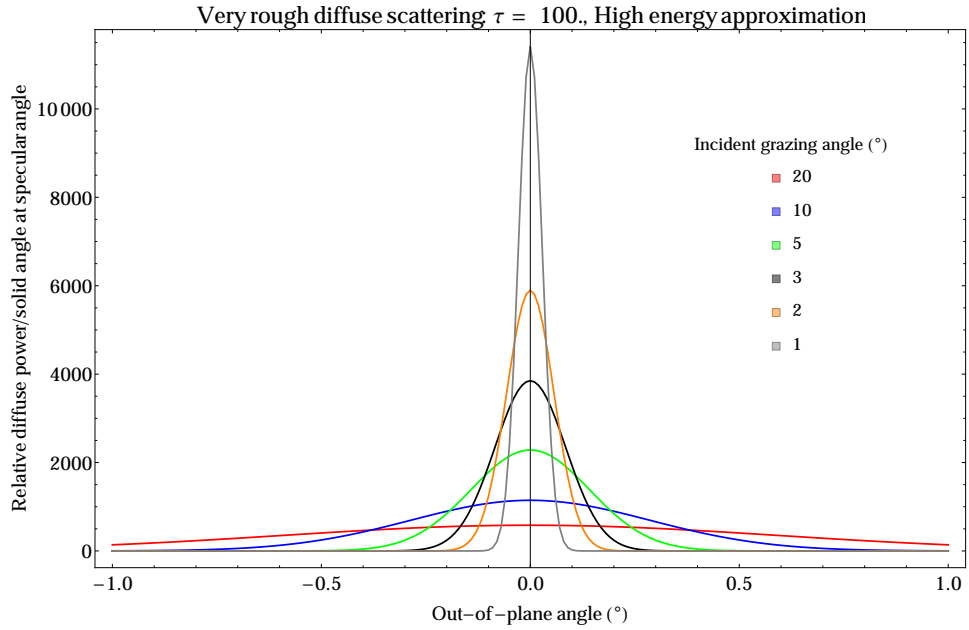


FIG. 6. Diffuse scattering out-of-plane reflected angle distributions for high energy photons. The curves are calculated from the approximate relation given in Eq. 15.

B. Diffuse reflection

The theory of diffuse scattering of electromagnetic waves from random rough surfaces is a well-developed subject, and is covered in detail in references [5] and [6]. The model used in **Synrad3D** and described in this paper is based on scalar Kirchhoff theory. This model has been used successfully to describe the scattering of soft X-rays from metal surfaces [8, 9]. The surface variation is assumed to be described by stochastic functions. For the surface height variation, the distribution is Gaussian, with rms σ . For the transverse distribution (the same in both transverse directions), the autocorrelation function is taken to have the form

$$C(s) = e^{-s^2/T^2} \quad (3)$$

in which s is a transverse distance and the autocorrelation coefficient is T . The surface roughness parameters σ and T , which characterize the surface deviations from a perfect plane, may be determined from measurements of the microstructure of the vacuum chamber surface, for example, using an atomic force microscope.

The most general expression for the diffusely reflected power fraction involves an infinite sum. The expression is

$$\frac{dF_{\text{diff}}}{d\Omega} = \frac{J(y, \lambda, x, \phi)}{J_0(y, \lambda)}, \quad (4)$$

in which

$$J(y, \lambda, x, \phi) = \frac{(1 + xy)^2}{(x + y)^4} (1 - a \cos \phi)^2 g e^{-g} \sum_{m=1}^{\infty} X_m, \quad (5)$$

$$g = \frac{4\pi^2 \sigma^2 (x + y)^2}{\lambda^2}, \quad (6)$$

$$X_m = \frac{g^m}{m!m} e^{-gq/m}, \quad (7)$$

$$q = \frac{(2 - x^2 - y^2 - 2h \cos \phi) \tau^2}{4(x + y)^2}, \quad (8)$$

$$\tau = \frac{T}{\sigma}, \quad (9)$$

$$h = \sqrt{1 - (x^2 + y^2) + x^2 y^2}, \text{ and} \quad (10)$$

$$a = \frac{h}{1 + xy}. \quad (11)$$

$$(12)$$

The normalization constant $J_0(y, \lambda)$ is given by

$$J(y, \lambda) = \int_0^1 dx \int_{-\pi}^{\pi} d\phi J(y, \lambda, x, \phi), \quad (13)$$

so that

$$\int_0^1 dx \int_{-\pi}^{\pi} d\phi \frac{dF_{\text{diff}}}{d\Omega} = 1 \quad (14)$$

This full expression is used in **Synrad3D**, and in all the comparisons with data made in this paper.

The expression simplifies substantially in the limit $g \gg 1$. This condition is satisfied for very rough surfaces, corresponding to technical vacuum chambers, and for high energy photons, for which typically $\sigma \gg \lambda$. In this limit, the differential fraction of diffusely reflected radiation is given by

$$\frac{dF_{\text{diff}}}{d\Omega} \approx \frac{J_a(y, x, \phi)}{J_{a0}(y)} \quad (15)$$

in which

$$J_a(y, x, \phi) = \frac{(1 + xy)^2}{(x + y)^4} (1 - a \cos \phi)^2 e^{-q}, \quad (16)$$

$$J_{a0}(y) = \int_0^1 dx \int_{-\pi}^{\pi} d\phi J_a(y, x, \phi). \quad (17)$$

In this limit, the differential fraction of diffusely reflected radiation is independent of λ , and depends on the surface only through the parameter τ .

Diffuse scattering distributions for 30 eV photons are shown in Fig. 3 and Fig. 4, for $\sigma = 100$ nm and $\tau = 100$. At this low photon energy, the approximation $g \gg 1$ does not hold in general, and the full diffuse scattering formalism (Eq. 4) is used to compute these distributions. For comparison, diffuse scattering distributions for high energy photons, for which $g \gg 1$ are shown in Fig. 5 and Fig. 6. These distributions have been computed from Eq. 15.

III. CHARACTERIZATION OF TECHNICAL ACCELERATOR VACUUM CHAMBER SURFACES

A. AFM image scans

The surface features of samples of technical accelerator vacuum chamber surfaces were characterized using an AFM (atomic force microscope). This microscope allowed measure-

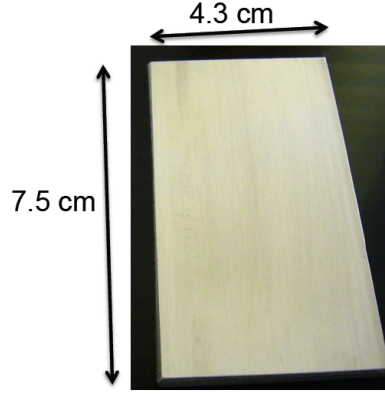


FIG. 7. Photograph of one of the aluminum vacuum chamber samples (Sample #1). The beam direction is parallel to the 7.5 cm long edge.

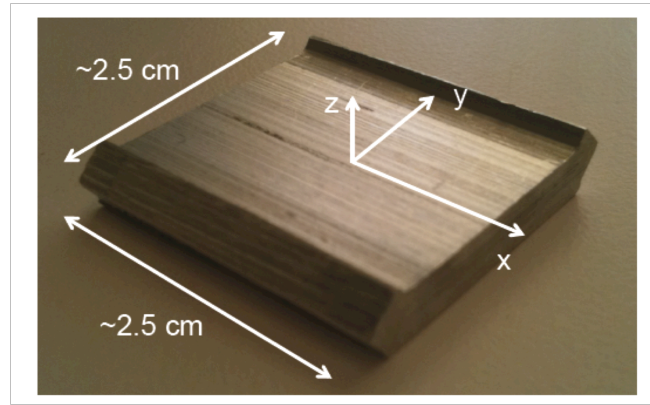


FIG. 8. Photograph of one of the aluminum vacuum chamber samples (Sample #2). The beam direction is along x . Note the distinct “ridges” which run parallel to the x -direction.

ments to be made of surface features on the scale of tens of nanometers up to tens of microns. Measurements were made for two samples of extruded aluminum chamber surfaces. Fig. 7 and Fig. 8 show the aluminum samples. Sample #2 clearly shows a pattern of visible ridges on the surface, which presumably is a consequence of the extrusion process used to fabricate the chamber. Sample #1 was also extruded, but looks much smoother to the naked eye.

A single AFM measurement consisted of a surface image scan of an area $20\text{ }\mu\text{m}$ by $20\text{ }\mu\text{m}$. A typical scan for sample #1 is shown in Fig. 9, and for sample #2 in Fig. 10. Superimposed

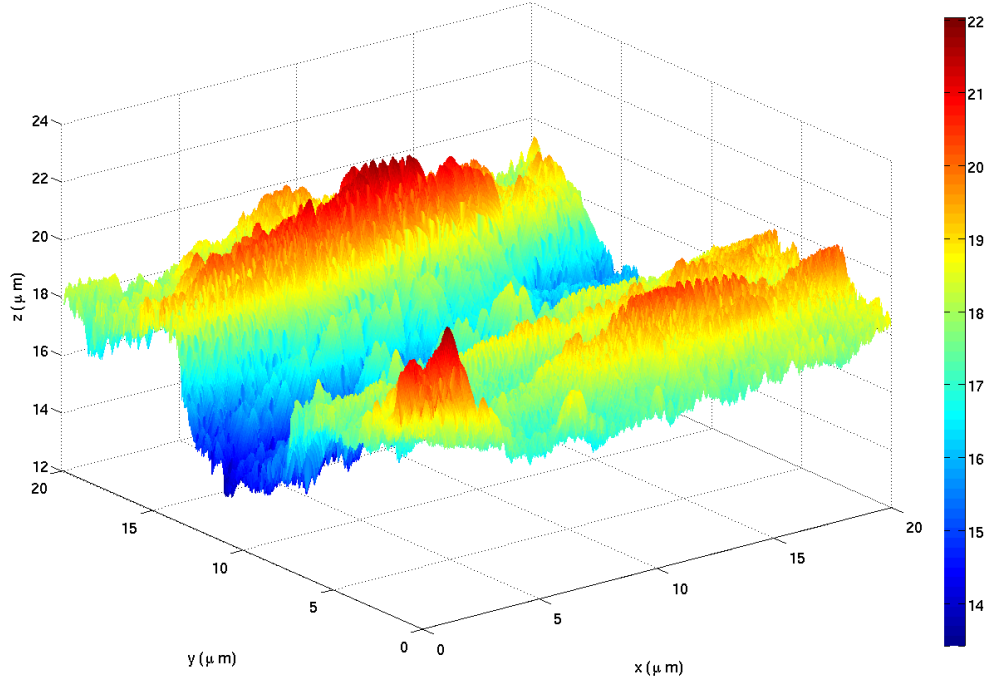


FIG. 9. Raw surface image scan of a $20\ \mu\text{m}$ by $20\ \mu\text{m}$ area of aluminum sample #1.

on a random pattern of surface roughness at the hundred-nanometer scale is a systematic long-wavelength (micron scale) surface height variation in the y -direction. The period of this long-wavelength variation appears to be of order $5\ \mu\text{m}$ for sample #1, and of order $20\ \mu\text{m}$ for sample #2. This can also be seen in Fig. 11, in which 6 adjacent scans are merged for sample #1, and in Fig. 12, in which 9 adjacent scans are merged for sample #2. For sample #1, the systematic surface variation has an amplitude of order $2\text{-}3\ \mu\text{m}$. For sample #2, the systematic surface variation has an amplitude of order $10\ \mu\text{m}$. These “grooves”, which are evident in the AFM scans, are too small to be seen by the naked eye. They should not be confused with the “ridges” shown in Fig. 8, which are visible to the naked eye. These features have a wavelength of order $500\ \mu\text{m}$, too long to be seen in the AFM scans.

To allow an analysis of the short-wavelength random roughness, the surface profile in the y -direction has been fit to a cubic polynomial to model the long-wavelength features, and the residuals of the fit have been extracted for the analysis described in the next section.

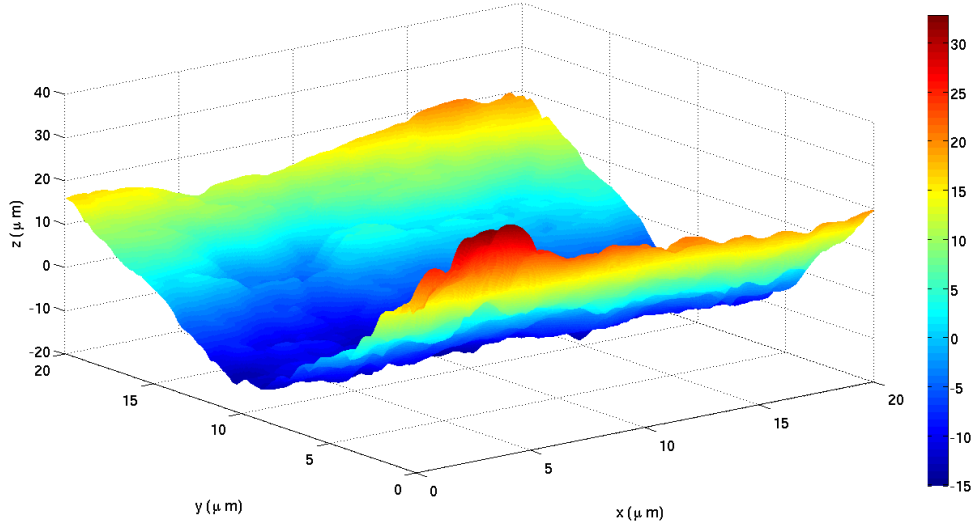


FIG. 10. Raw surface image scan of a $20\ \mu\text{m}$ by $20\ \mu\text{m}$ area of aluminum sample #2.

B. Analysis of image scans to extract surface roughness parameters

For each sample, a series of 9 image scans were made, as discussed in the previous section. The rms surface height variation and the autocorrelation function for the surface were computed. Fig. 13 shows the height variation and autocorrelation function for one of the image scans. To extract the autocorrelation coefficient T , the autocorrelation function was fit to the form shown in Eq. 3. As Fig. 13 shows, the measured autocorrelation function is slightly different from a Gaussian.

The average values and standard deviation for the surface roughness parameters from the scans are presented in Tab. I. For the y -direction, the numbers correspond to an analysis of the surface residuals after subtraction of the cubic polynomial. For aluminum sample #1, the average and variance for 6 image scans is shown. For aluminum sample #2, two different sets of 9 image scans were made, in two different locations on the sample, and the average and variance in the 18 data sets is shown.

For the aluminum samples, the AFM measurements (after subtracting the cubic fit) are consistent with a value of σ around 100 nm, for both transverse directions and both samples, with variances ranging from 6% to 25%. However, the values for the autocorrelation coefficient are less well determined. The values of T for the two samples range from about $3.4\ \mu\text{m}$ to about $17\ \mu\text{m}$; the corresponding values of the ratio τ range from 34 to 213, with

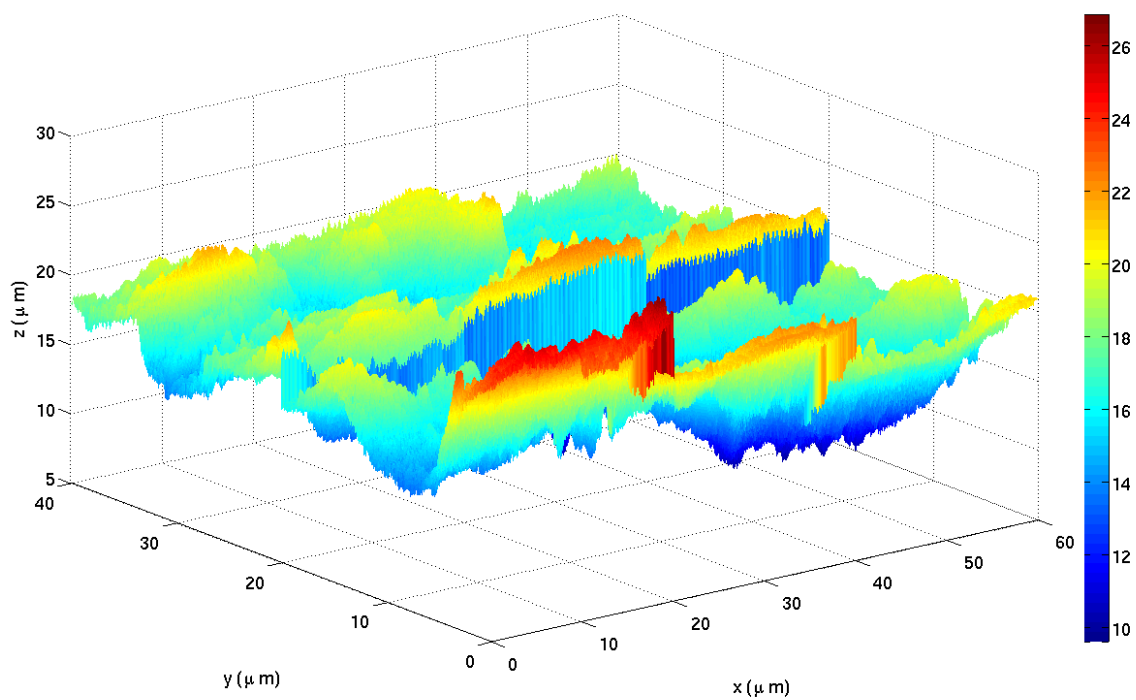


FIG. 11. Merge of 6 adjacent images scans for aluminum sample #1.

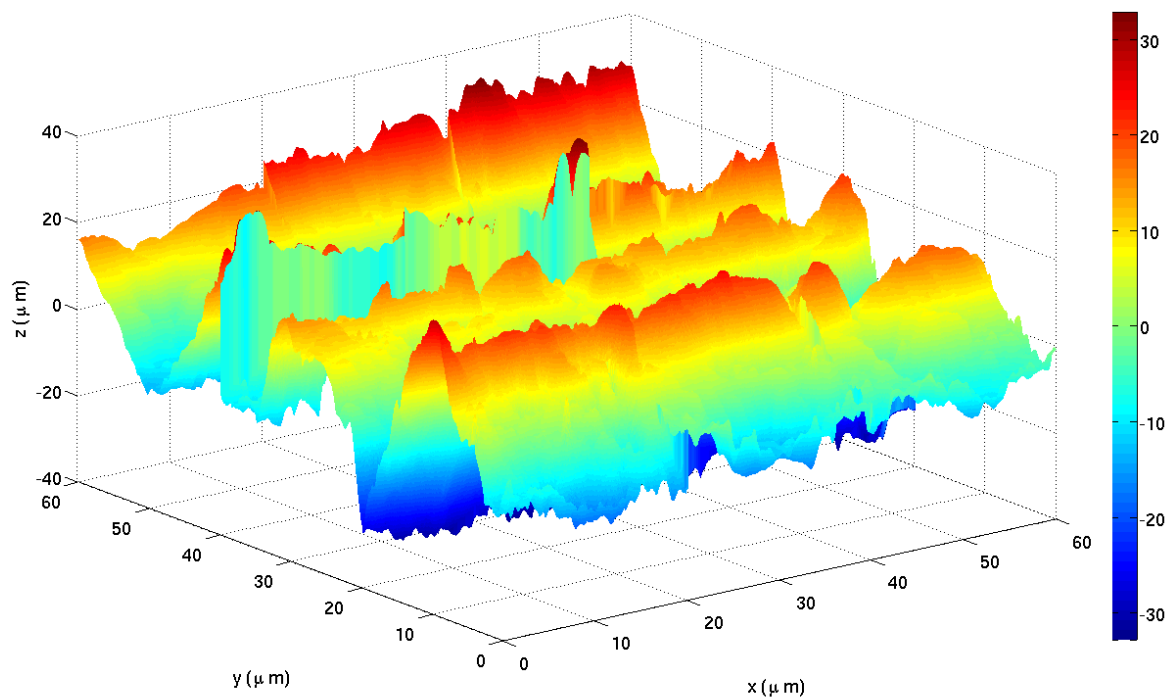


FIG. 12. Merge of 9 adjacent images scans for aluminum sample #2.

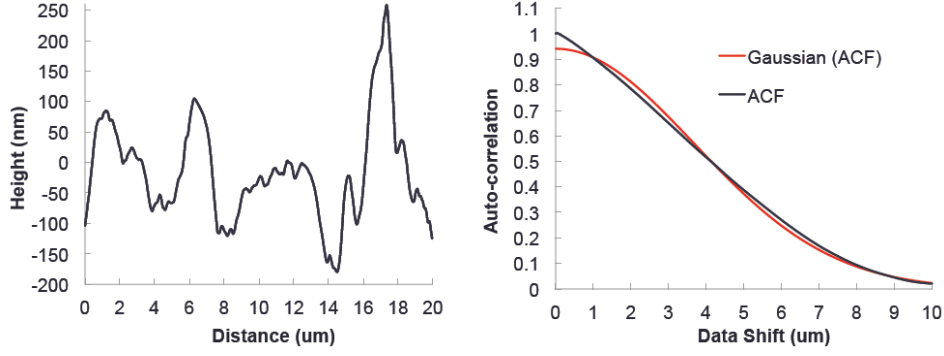


FIG. 13. Height variation and autocorrelation function for one of the image scans. The red line is the best fit to a Gaussian autocorrelation function. The autocorrelation coefficient for this fit is $T = 5.2 \mu\text{m}$.

Chamber sample	σ_x	T_x	τ_x	σ_y	T_y	τ_y
	(nm)	(nm)		(nm)	(nm)	
Al#1	97	14896	166	93	17080	213
Al#1 Variance	24	5712	76	24	11185	169
Al#2	101	8175	81	102	3425	34
Al#2 Variance	6	3848	33	17	828	9

TABLE I. Measured surface roughness parameters, for x and y direction. For the y -direction, the numbers correspond to an analysis of the surface residuals after subtraction of a cubic polynomial. The averages and variances are computed from the results for 6 image scans for sample #1, and 18 image scans for sample #2.

variances of as much as 80% for sample #1.

In the analysis described below for the X-ray scattering angular distributions from aluminum sample #1, we will take σ to be 95 nm, based on the AFM measurements. However, since τ is not well determined from the AFM data, we will allow it to be a free parameter in the fits.

IV. X-RAY SCATTERING MEASUREMENTS

A. Experimental setup

The X-ray scattering measurements on the samples described in the previous section were done using the UHV triple axis soft X-ray reflectometer[10] at the BESSY II synchrotron. The detector is a GaAsP photodiode, located 150 mm from the sample, which can scan the scattering angle (in the vertical scattering plane) as well as out-of-plane angles. The incident photon energy is controlled by a grating monochromator. The low-energy grating allows the energy to be varied from 20 to 150 eV, and the high-energy grating allows energies from 150 to 1500 eV. A schematic of the sample setup is shown in Fig. 14. The angle θ_1 is the grazing angle of incidence. The angle θ_2 is the total scattering angle from the photon beam direction, i.e, the grazing angle of incidence plus the grazing angle of reflection. The angle ϕ is the angle of scattering out of the plane of incidence.

B. Characterization of the detector and the photon beam

1. Energy response

To characterize the energy response of the system, measurements were made with no sample in place, and with the detector set to $\theta_2 = \phi = 0$. Using the low-energy grating, the beam energy was scanned from about 20 eV to about 150 eV. The “normalized photocurrent” (photocurrent measured by the detector, divided by the ring current), is presented in Fig. 15. Similarly, Fig. 16 illustrates a scan from about 150 eV to 1500 eV, using the high energy grating. These curves are proportional to the product of the energy spectrum of the photon beam (as filtered by the grating) times the detector efficiency at that energy.

2. Angular response: reflected grazing angle

The angular response E_θ of the detector for the reflected grazing angle was measured by scanning the normalized photocurrent measured by the detector in θ_2 with no sample in place, with $\phi = 0$. A scan of this form is shown in Fig. 17, for a beam energy of 180 eV. To model this, we use a functional form corresponding to the convolution of a Gaussian with

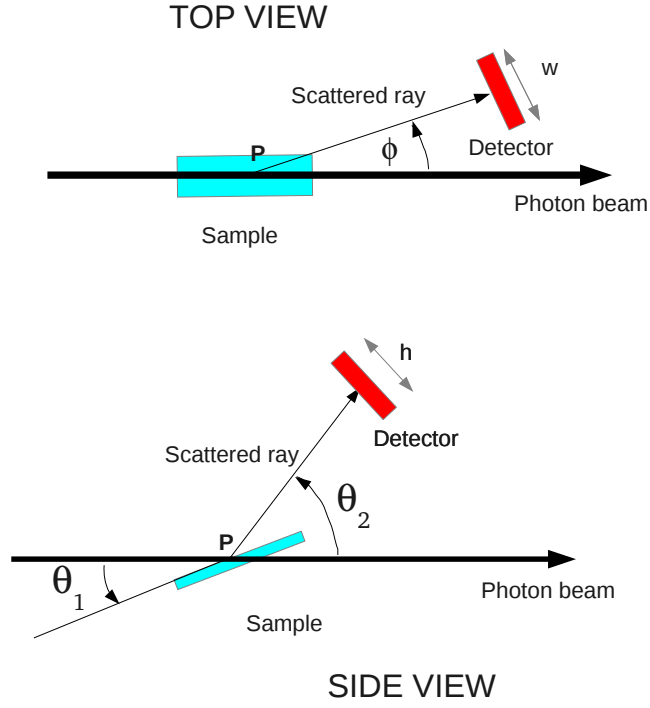


FIG. 14. Experimental setup, showing key angle observables.

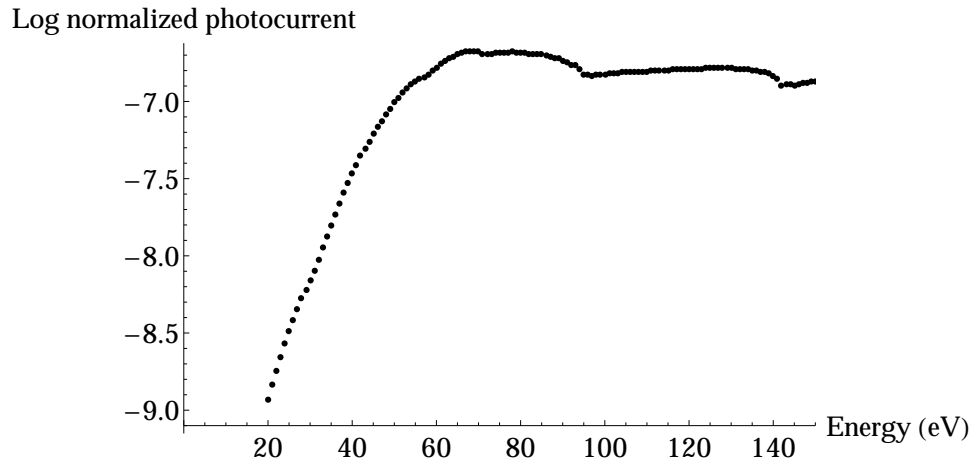


FIG. 15. Scan of normalized detector response with no sample vs. energy, using the low energy monochromator, with $\theta_2 = \phi = 0$.

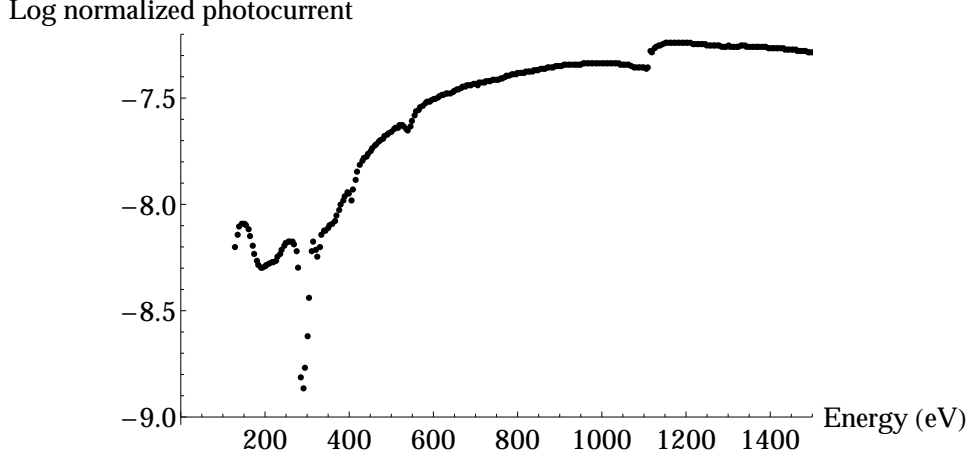


FIG. 16. Scan of normalized detector response with no sample vs. energy, using the high energy monochromator, with $\theta_2 = \phi = 0$.

rms width σ_{vb} (proportional to the beam vertical width) with a rectangular distribution of half-width θ_v (proportional to the vertical height of the detector):

$$E_\theta(\theta_2) = S(\theta_2, \theta_v, \sigma_{vb}, \sigma_{vb}) \quad (18)$$

in which

$$S(x, x_0, \sigma_1, \sigma_2) = \frac{\left(\operatorname{erf}\left(\frac{x+x_0}{\sqrt{2}\sigma_1}\right) - \operatorname{erf}\left(\frac{x-x_0}{\sqrt{2}\sigma_1}\right) \right)}{2 \operatorname{erf}\left(\frac{x_0}{\sqrt{2}\sigma_2}\right)} \quad (19)$$

Photon energy	$\theta_v(^{\circ})$	$\sigma_{vb}(^{\circ})$	offset ($^{\circ}$)
180 eV	0.836 ± 0.00016	0.0389 ± 0.00023	-0.1317 ± 0.0002
20 eV	0.840 ± 0.015	0.0844 ± 0.011	-0.021 ± 0.02
20 eV	0.833 ± 0.0025	0.050 ± 0.0042	-0.061 ± 0.002
20 eV	0.837 ± 0.001	0.0426 ± 0.0014	-0.059 ± 0.001
Average	0.837	0.039	

TABLE II. Summary of fits to no-sample detector scans in θ_2 . An overall offset from $\theta_2 = 0$, shown in the third column, was also a free parameter in the fit.

A summary of the results of this fitting procedure for scans with different energies is presented in Table II. The weighted average of the fit parameters is also given in this table. The average value of θ_v is 0.837° , and the average value of σ_{vb} is 0.039° . Using the fact that

the distance from the detector pivot point (“P” in Fig. 14) to the detector is 150 mm, we can deduce that the effective detector height (h in Fig. 14) is 4.4 mm, and the rms vertical beam size is 0.10 mm.

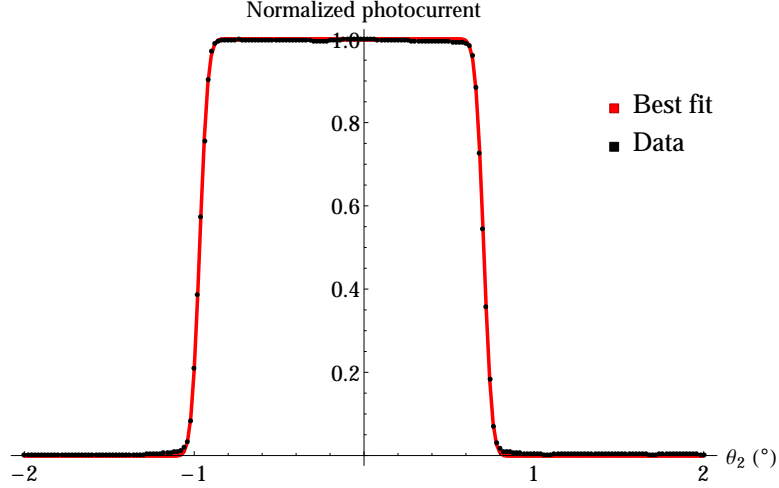


FIG. 17. Scan of normalized detector response vs. θ_2 with no sample, using a 180 eV photon beam. The red curve is the best fit, using Eq. 19.

3. Angular response: out-of-plane reflected angle

Similarly, a scan in ϕ of the normalized detector photocurrent with no sample in place is shown in Fig. 18. This scan gives the out-of-plane angular response function E_ϕ . To model this, we again use a functional form corresponding to the convolution of a Gaussian with rms width σ_{hb} (proportional to the beam horizontal width) with a rectangular distribution of half-width ϕ_h (proportional to the width of the detector):

$$E_\phi(\phi) = S(\phi, \phi_h, \sigma_{hb}, \sigma_{hb}) \quad (20)$$

A summary of the results of this fitting procedure for scans with different energies is presented in Table III. The weighted average of the fit parameters is also given in this table. The average value of ϕ_h is 1.13° , and the average value of σ_{hb} is 0.162° . Using the fact that the distance from the pivot point to the detector is 150 mm, we can deduce that the effective detector height (w in Fig. 14) is 5.9 mm, and the rms horizontal beam size is 0.42 mm.

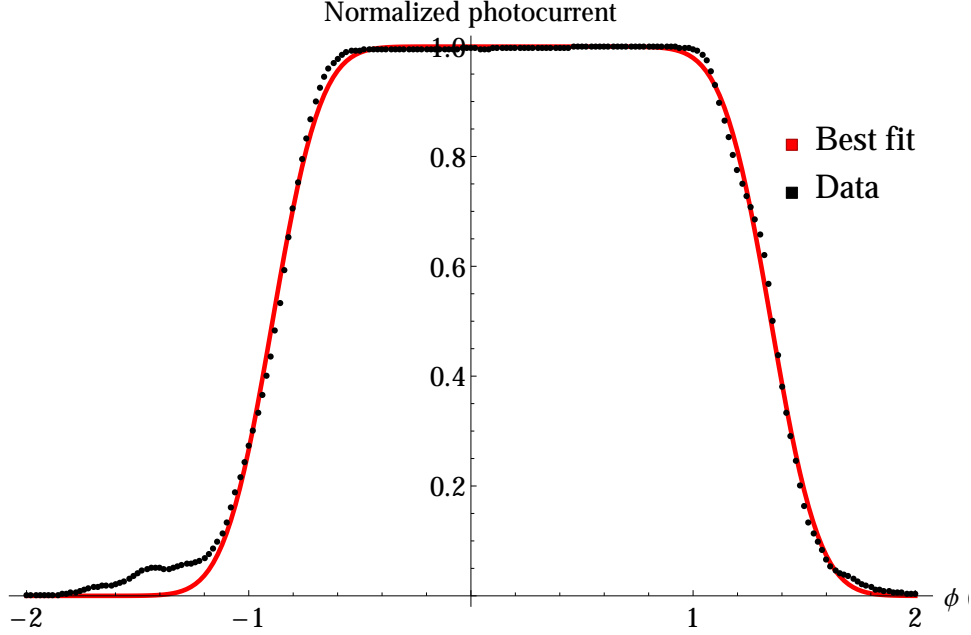


FIG. 18. Scan of detector response vs. ϕ with no sample, using a 180 eV photon beam. The red curve is the best fit, using Eq. 20.

Photon energy	$\phi_h(^{\circ})$	$\sigma_{hb}(^{\circ})$	offset ($^{\circ}$)
180 eV	1.12 ± 0.0015	0.172 ± 0.0022	0.229 ± 0.002
20 eV	1.18 ± 0.015	0.128 ± 0.0147	-0.042 ± 0.018
20 eV	1.16 ± 0.0044	0.089 ± 0.0062	-0.091 ± 0.004
Average	1.13	0.162	

TABLE III. Scan of detector response vs. ϕ with no sample, using a 180 eV photon beam. An overall offset from $\phi = 0$, shown in the third column, was also a free parameter in the fit.

C. Experimental results from aluminum samples

1. Energy Scans: Aluminum sample #1

For these scans, the detector position is fixed, and the photon beam energy is varied, using either the low-energy or the high-energy grating. The low-energy scans cover the

range from about 20 to 150 eV. The high-energy scans range from 150 to about 1500 eV. A summary of the data sets is presented in Table IV.

Data set	Energy	$\theta_1(^{\circ})$	$\theta_2(^{\circ})$
E1	Low	3	5.2
E2	Low	5	9
E3	Low	10	19
E4	High	1.5	3
E5	High	1.5	2.6
E6	High	3	5.2
E7	High	5	9.4

TABLE IV. Table of energy scan data sets, for aluminum sample #1. The out-of-plane angle is fixed at $\phi = 0$.

The “observed reflectivity” (not corrected for the geometric efficiency of the detector) may be obtained from these scans by dividing the reflected normalized photocurrent by the incident normalized photocurrent, which is given in Fig. 15 and Fig. 16. The observed reflectivity data are shown in Fig. 19. Inspection of the figure reveals an inconsistency between the low-energy scans and the high-energy scans. The data points in data sets E1 and E6, corresponding to the same values of θ_1 and θ_2 , measured in the region of energy overlap between the scans (about 150 eV), do not agree. This is indicated by the discontinuity in the red curve in Fig. 19. Similarly, the data points in data sets E2 and E7, corresponding to the same values of θ_1 and slightly different values of θ_2 , measured in the energy overlap region (about 150 eV), also are in major disagreement. This is indicated by the discontinuity in the blue curves in the energy range near 150 eV, as shown Fig. 19. These inconsistencies indicate some problem with the absolute normalization of either the low-energy scan or the high-energy scan (or both).

Apart from the issue of the absolute normalization of the observed reflectivity measurements, Fig. 19 shows clear evidence for absorption edges at several energies. The L-edges of aluminum, in the range of 75-90 eV, are clearly visible, as is the aluminum K-edge at around 1560 eV. The data also show evidence for the K-edge of carbon, at about 280 eV, and the K-edge of oxygen, around 530 eV.

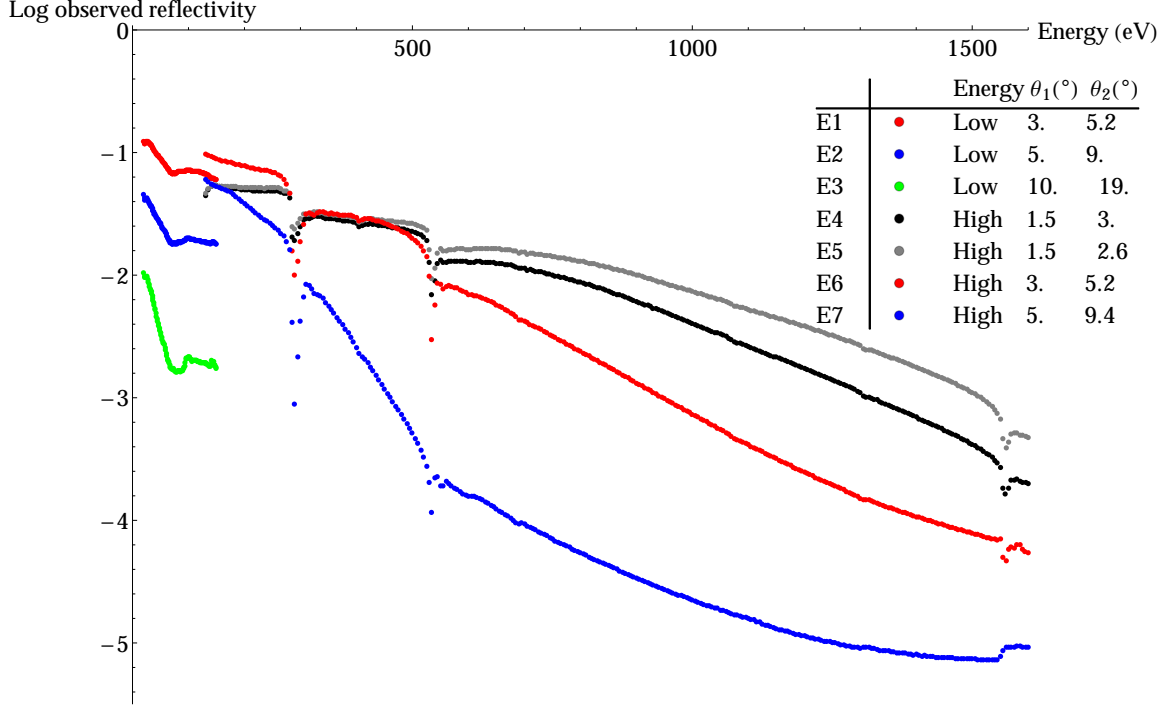


FIG. 19. Observed reflectivity, as a function of energy, aluminum sample #1.

2. Energy Scans: Aluminum sample #2

A summary of the energy scan data sets for aluminum sample #2 is presented in Table V.

Data set	Energy	$\theta_1(^{\circ})$	$\theta_2(^{\circ})$
F1	Low	1.5	2.4
F2	Low	3	4
F3	Low	5	8
F4	Low	10	17
F5	Low	20	37
F6	High	1.5	2.6
F7	High	3	5
F8	High	5	6.4

TABLE V. Table of energy scan data sets, for aluminum sample #2. The out-of-plane angle is fixed at $\phi = 0$.

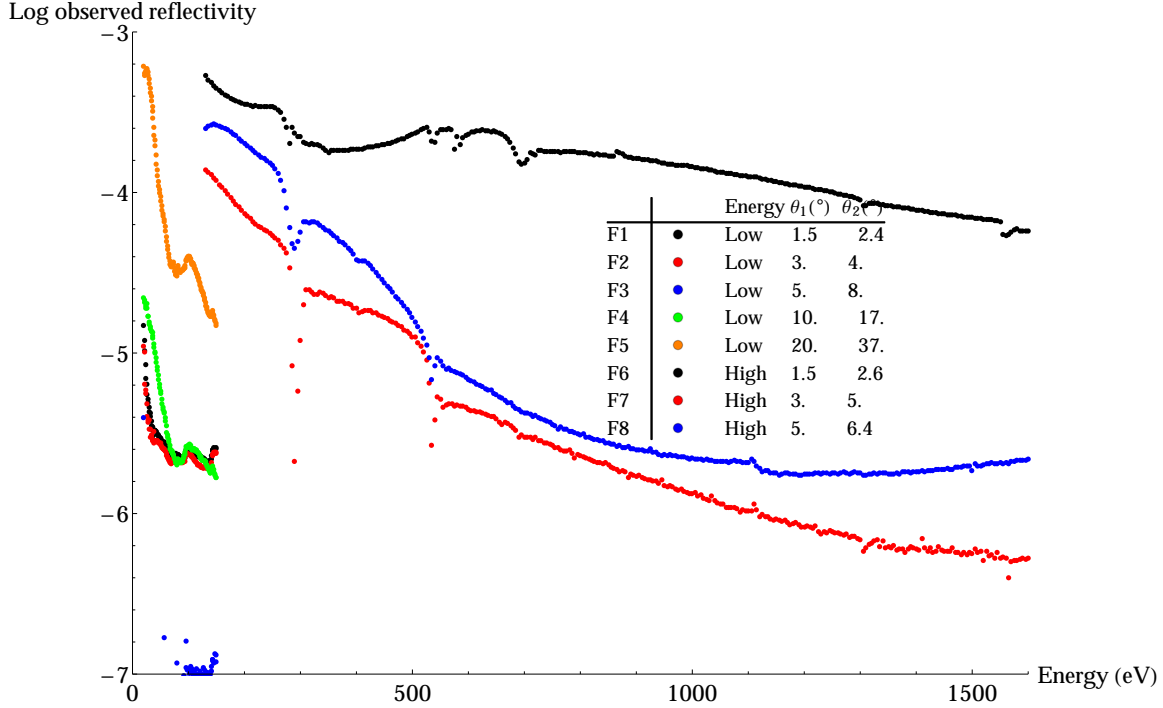


FIG. 20. Observed reflectivity, as a function of energy, aluminum sample #2.

The observed reflectivity data are shown in Fig. 20. Comparison with Fig. 19 shows immediately that the reflectivity for this sample is two to three orders of magnitude lower than the reflectivity of sample #1. In addition, the same discontinuities between the low- and high-energy scans, in the region of their mutual energy overlap, is seen here. Additionally, the low-energy scans indicate a much higher reflectivity for $\theta_1 = 20^{\circ}$ than for smaller angles, which is not expected. Fig. 20 exhibits similar X-ray edge features as sample #1.

3. Hypothesis regarding long-wavelength surface features

As will be presented below, the observed reflectivity for sample #1 is considerably smaller than would be expected from the smooth surface reflectivity values (after correction for detector efficiency) obtained from the LBNL database (see Fig. 1). For sample #2, the observed reflectivity is further reduced by 2 to 3 orders of magnitude. The hypothesis in this paper, which is discussed in more detail below, is that the long-wavelength surface features resulting from the extrusion process, visible in Fig. 8 for sample #2, are responsible for the dramatic suppression of the observed reflectivity. These features, quite prominent in sample #2, are less pronounced in sample #1, which looks much smoother to the naked

eye (see Fig. 7). The less prominent long-wavelength surface features in sample #1 result in this sample having a higher reflectivity.

In the remaining sections of this paper, we will focus on the reflectivity measurements, and on the measurements of angular distributions for sample #1. Angular distributions were also measured for sample #2, but, because of its very low reflectivity, many of the distributions for small grazing angles are contaminated with tails from the direct beam. The shape of the angular distributions for sample #1 will be compared with the predictions of the scattering model presented in Sec. II. The reflectivity measurements of sample #1 and sample #2 will be compared with the predictions of a simple model based on geometric scattering from a grooved surface such as that shown in Fig. ??.

4. *Reflected grazing angle scans*

For these scans, the photon beam energy, the out-of-plane angle, and the sample's angle relative to the beam (θ_1), are fixed. The detector angle θ_2 is varied. A summary of the data sets is presented in Table VI. The last columns in this table give the maximum value of the normalized photocurrent measured during each scan, and the angle at which the maximum occurs. To plot the data, the normalized photocurrent has been divided by this maximum value, to give the “rescaled normalized photocurrent”, which ranges from 0 to 1. The plots corresponding to the data sets shown in Table VI are presented in Fig. 21 to Fig. 24.

5. *Reflected out-of-plane angle scans*

For these scans, the photon beam energy, the detector angle θ_2 , and the sample's angle relative to the beam (θ_1), are fixed. The out-of-plane angle ϕ is varied. A summary of the data sets is presented in Table VII. The last column in this table gives the maximum value of the normalized photocurrent measured during each scan. This maximum always occurs at $\phi = 0$. To plot the data, the normalized photocurrent has been divided by this maximum value, to give the “rescaled normalized photocurrent”, which ranges from 0 to 1. The plots corresponding to the data sets shown in Table VII are presented in Fig. 25.

Data set	Scan type	$\theta_1(^{\circ})$	Energy (eV)	Maximum	$\theta_2(^{\circ})$
				value	at maximum
Th1	θ_2	1.5	20	1.3×10^{-10}	2.6
Th2	θ_2	1.5	50	1.07×10^{-8}	2.6
Th3	θ_2	1.5	80	2.1×10^{-8}	2.6
Th4	θ_2	1.5	150	4.4×10^{-10}	2.6
Th5	θ_2	3.0	20	1.44×10^{-10}	5.2
Th6	θ_2	3.0	150	7.2×10^{-10}	5.2
Th7	θ_2	5.0	150	4.4×10^{-10}	9.4
Th8	θ_2	10.0	150	3.1×10^{-11}	18.2
Th9	θ_2	10.0	20	1.2×10^{-11}	19.0
Th10	θ_2	20.0	20	1.3×10^{-13}	39.5

TABLE VI. Table of θ_2 scan data sets, for aluminum sample #1. The out-of-plane angle is fixed at $\phi = 0$.

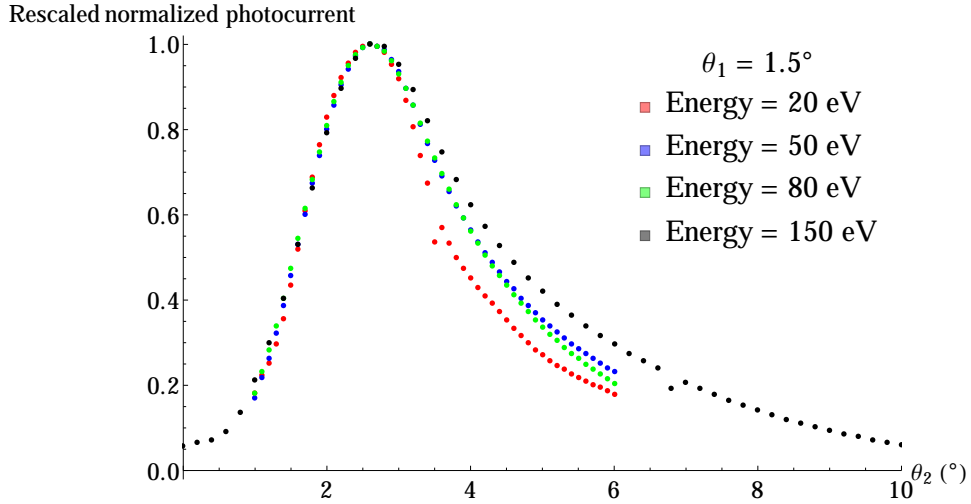


FIG. 21. Data sets Th1-Th4: scan of θ_2 for several energies, with fixed $\theta_1 = 1.5^{\circ}$, aluminum sample #1.

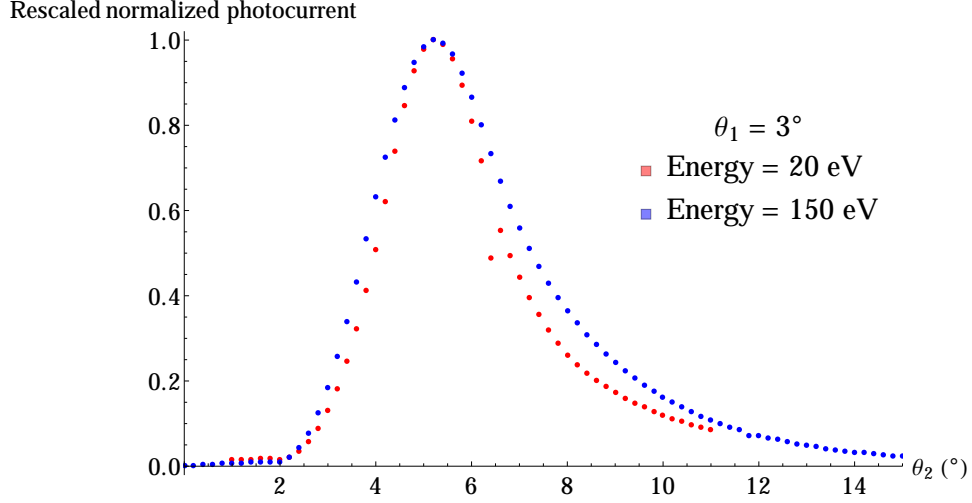


FIG. 22. Data sets Th5-Th6: scan of θ_2 for two energies, with fixed $\theta_1 = 3^\circ$, aluminum sample #1.

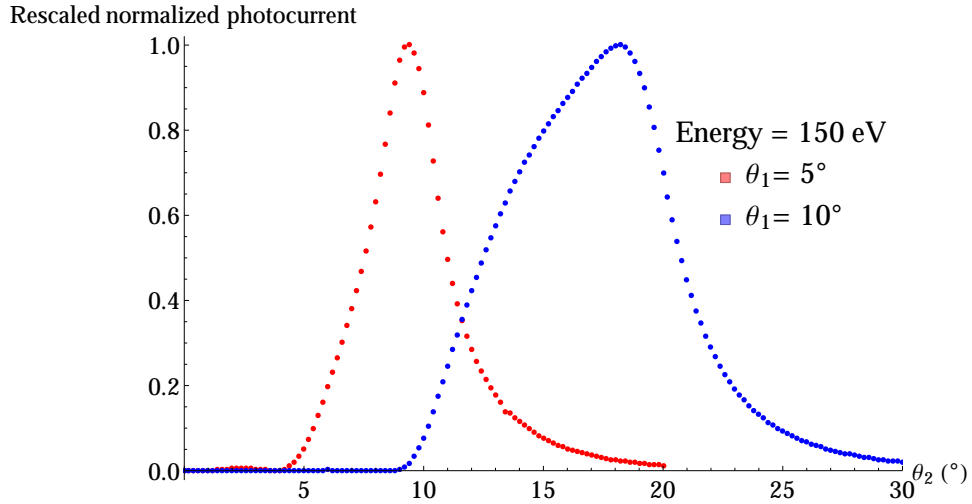


FIG. 23. Data sets Th7-Th8: scan of θ_2 for $\theta_1 = 5^\circ$ and $\theta_1 = 10^\circ$, energy 150 eV, aluminum sample #1.

Data set	Scan type	Energy (eV)	Maximum value
Ph1	ϕ	20	1.3×10^{-10}
Ph2	ϕ	50	1.1×10^{-8}
Ph3	ϕ	80	2.1×10^{-8}
Ph4	ϕ	130	1.6×10^{-8}

TABLE VII. Table of ϕ scan data sets, for aluminum sample #1. The angle θ_1 is fixed at 1.5° , and θ_2 is fixed at 2.6°

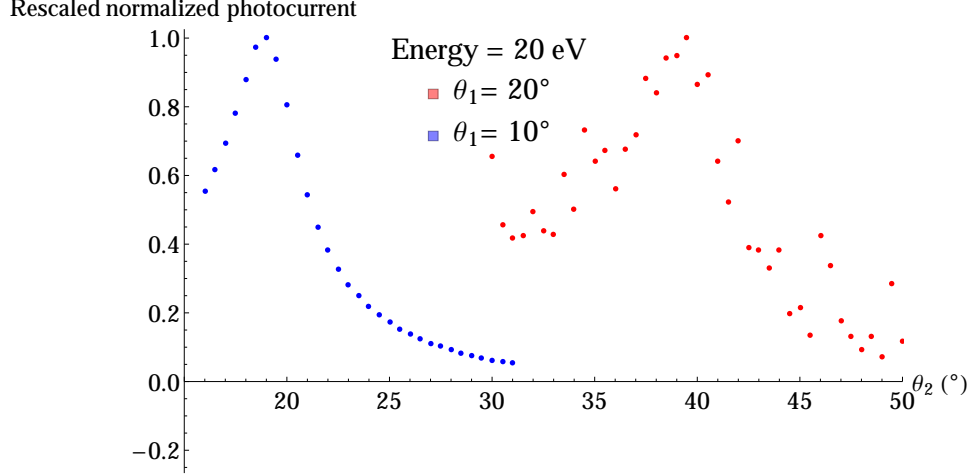


FIG. 24. Data sets Th9-Th10: scan of θ_2 for $\theta_1 = 10^\circ$ and $\theta_1 = 20^\circ$, energy 120 eV, aluminum sample #1

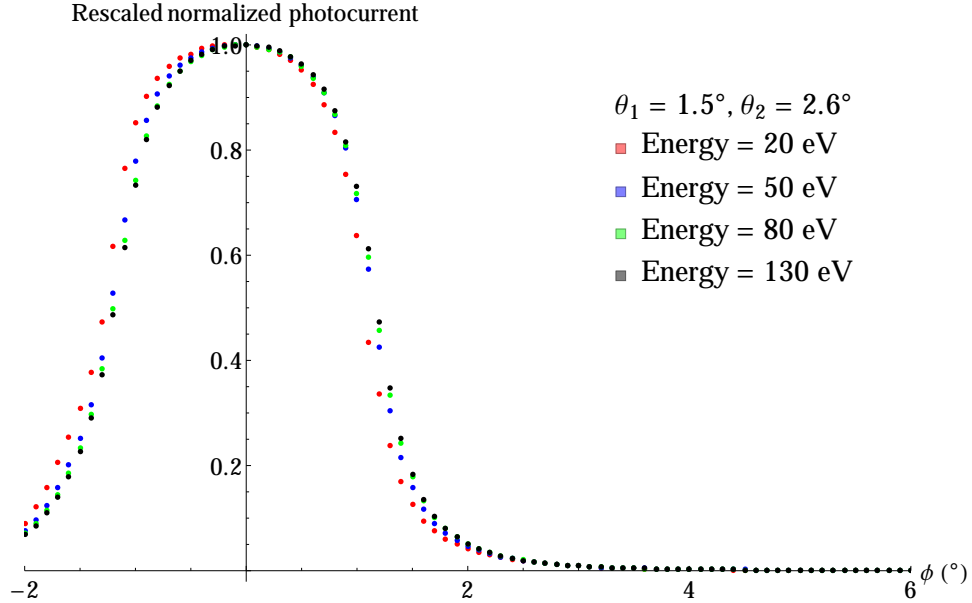


FIG. 25. Data sets Ph1-Ph4: scan of out-of-plane angle for several energies, with fixed $\theta_1 = 1.5^\circ$ and $\theta_2 = 2.6^\circ$, aluminum sample #1

V. COMPARISON BETWEEN THE THEORY AND THE MEASUREMENTS

A. Application of the scattering formalism to the measurements

To compare the theory presented in Sec. II with the measurements presented in Sec. IV C, we proceed as follows. The total differential number of photons dN reflected per unit solid

angle is proportional to the relative reflected power per unit solid angle (Eq. 1):

$$\frac{1}{N_0} \frac{dN}{d\Omega} = \frac{1}{P_0} \frac{dP_{\text{tot}}}{d\Omega} = G(y, \lambda, x, \phi) \quad (21)$$

in which N_0 is the incident number of photons, and the function G is defined from Eq. 1:

$$G(y, \lambda, x, \phi) = R(y, \lambda) \left(P_{\text{spec}}(y, \lambda) \delta(x - y) \delta(\phi) + (1 - P_{\text{spec}}(y, \lambda)) \frac{J(y, \lambda, x, \phi)}{J_0(y, \lambda)} \right). \quad (22)$$

As discussed in Sec. II, $y = \cos \psi_i$, the incident polar angle relative to the surface normal, and $x = \cos \psi_r$, the reflected polar angle relative to the surface normal. For comparison with the experimental data, it is convenient to change variables to $\theta_i = \pi/2 - \psi_i$, the incident grazing angle, and $\theta_r = \pi/2 - \psi_r$, the reflected grazing angle.

In principle, the experimental observable θ_1 should be equal to the grazing angle of incidence θ_i . In practice, there is an experimental setting error, which makes θ_1 differ from θ_i . We assume that

$$\theta_i = \hat{\theta}_1(\theta_1)$$

in which

$$\hat{\theta}_1(x) = a + bx + cx^2$$

The parameters a , b , and c , assumed to be the same for all the angular scan data sets, are determined during the data fitting described below.

The experimental observable θ_2 is equal to the sum of the grazing reflected angle θ_r and the grazing angle of incidence θ_i . Thus

$$\theta_r = \theta_2 - \theta_i = \theta_2 - \hat{\theta}_1.$$

Then we have

$$y = \cos(\pi/2 - \theta_i) = \cos(\pi/2 - \hat{\theta}_1) \quad (23)$$

$$x = \cos(\pi/2 - \theta_2 + \hat{\theta}_1) \quad (24)$$

The differential transforms as

$$dx = d \cos(\pi/2 - \theta_2 + \hat{\theta}_1) = \cos(\theta_2 - \hat{\theta}_1) d\theta_2. \quad (25)$$

Thus, in terms of the experimental observables, we have

$$\begin{aligned} \frac{d^2 N}{d\phi d\theta_2} &= N_0 \cos(\theta_2 - \hat{\theta}_1) G(\cos(\pi/2 - \hat{\theta}_1), \lambda, \cos(\pi/2 - \theta_2 + \hat{\theta}_1), \phi) \\ &= N_0 \cos(\theta_2 - \hat{\theta}_1) G(\sin \hat{\theta}_1, \lambda, \sin(\theta_2 - \hat{\theta}_1), \phi) \\ &= N_0 R(\sin \hat{\theta}_1, \lambda) H(\hat{\theta}_1, \lambda, \theta_2, \phi) \end{aligned} \quad (26)$$

in which

$$\begin{aligned}
H(\hat{\theta}_1, \lambda, \theta_2, \phi) &= \cos(\theta_2 - \hat{\theta}_1) \left(P_{\text{spec}}(\sin \hat{\theta}_1, \lambda) \delta(\sin(\theta_2 - \hat{\theta}_1) - \sin \hat{\theta}_1) \delta(\phi) + \right. \\
&\quad \left. \left(1 - P_{\text{spec}}(\sin \hat{\theta}_1, \lambda) \right) \frac{J(\sin \hat{\theta}_1, \lambda, \sin(\theta_2 - \hat{\theta}_1), \phi)}{J_0(\sin \hat{\theta}_1, \lambda)} \right) \\
&= H_{\text{spec}}(\hat{\theta}_1, \lambda, \theta_2, \phi) + H_{\text{diff}}(\hat{\theta}_1, \lambda, \theta_2, \phi)
\end{aligned} \tag{27}$$

in which

$$\begin{aligned}
H_{\text{spec}}(\hat{\theta}_1, \lambda, \theta_2, \phi) &= P_{\text{spec}}(\sin \hat{\theta}_1, \lambda) \cos(\theta_2 - \hat{\theta}_1) \delta(\sin(\theta_2 - \hat{\theta}_1) - \sin \hat{\theta}_1) \delta(\phi) \\
&= P_{\text{spec}}(\sin \hat{\theta}_1, \lambda) \delta(\theta_2 - 2\hat{\theta}_1) \delta(\phi)
\end{aligned} \tag{28}$$

and

$$H_{\text{diff}}(\hat{\theta}_1, \lambda, \theta_2, \phi) = \left(1 - P_{\text{spec}}(\sin \hat{\theta}_1, \lambda) \right) \frac{J(\sin \hat{\theta}_1, \lambda, \sin(\theta_2 - \hat{\theta}_1), \phi)}{J_0(\sin \hat{\theta}_1, \lambda)} \cos(\theta_2 - \hat{\theta}_1) \tag{29}$$

For a given setting of the detector angles θ_2 and ϕ , the total number of photons detected N_{det} will be given by the convolution of the differential number distribution with the angular response functions of the detector, times $\epsilon(\lambda)$, the efficiency of the detector for detecting photons of wavelength λ :

$$\begin{aligned}
N_{\text{det}}(\hat{\theta}_1, \lambda, \theta_2, \phi) &= N_0 \epsilon(\lambda) R(\sin \hat{\theta}_1, \lambda) \int d\theta'_2 \int d\phi' H(\theta_1, \lambda, \theta'_2, \phi') E_\theta(\theta_2 - \theta'_2) E_\phi(\phi - \phi') \\
&= N_{\text{spec}}(\hat{\theta}_1, \lambda, \theta_2, \phi) + N_{\text{diff}}(\hat{\theta}_1, \lambda, \theta_2, \phi)
\end{aligned} \tag{30}$$

in which

$$N_{\text{spec}}(\hat{\theta}_1, \lambda, \theta_2, \phi) = N_0 \epsilon(\lambda) R(\sin \hat{\theta}_1, \lambda) P_{\text{spec}}(\sin \hat{\theta}_1, \lambda) E_\theta(\theta_2 - 2\hat{\theta}_1) E_\phi(\phi) \tag{31}$$

and

$$\begin{aligned}
N_{\text{diff}}(\hat{\theta}_1, \lambda, \theta_2, \phi) &= N_0 \epsilon(\lambda) \frac{R(\sin \hat{\theta}_1, \lambda) (1 - P_{\text{spec}}(\sin \hat{\theta}_1, \lambda))}{J_0(\sin \hat{\theta}_1, \lambda)} \\
&\quad \int d\theta'_2 \int d\phi' J(\sin \hat{\theta}_1, \lambda, \sin(\theta'_2 - \hat{\theta}_1), \phi') \cos(\theta'_2 - \hat{\theta}_1) E_\theta(\theta_2 - \theta'_2) E_\phi(\phi - \phi')
\end{aligned} \tag{32}$$

B. Modification for long-wavelength surface features

For some of the data sets corresponding to the lowest energies and smallest grazing angles, most of the scattering is specular, and so the measured angular distributions should

be very similar in shape to the angular response functions measured with no sample in place. However, this is not the case, as can be seen by examining Fig. 21 and Fig. 25.

The simplest explanation for this discrepancy is the presence of the long-wavelength surface features discussed in Sec. IV C 3 which introduce effective angular variations in the surface from a perfect plane. A simple model for the surface features is discussed below in Sec V F 2. This model indicates the scale of the expected angular variation (see Fig. 34). The distribution function for these angular features depends in detail on the surface features, which are not well known. For simplicity, we assume a Gaussian distribution for the angular variations, with an rms width obtained by fitting to the data.

We convolve the expressions for the angular response functions given in Sec. IV B with this Gaussian surface feature function, characterized by rms variations σ_{vs} in the θ_2 direction, and σ_{hs} in the ϕ direction:

$$F_s(\theta_2, \phi) = \frac{e^{\frac{-\theta_2^2}{2\sigma_{vs}^2}} e^{\frac{-\phi^2}{2\sigma_{hs}^2}}}{\sqrt{2\pi}\sigma_{vs} \sqrt{2\pi}\sigma_{hs}} \quad (33)$$

The convolution integral is

$$\int d\phi' \int d\theta'_2 S(\theta_2 - \theta'_2, \theta_v, \sigma_{vb}, \sigma_{vb}) S(\phi - \phi', \phi_h, \sigma_{hb}, \sigma_{hb}) F_s(\theta'_2, \phi') = \quad (34)$$

$$S(\theta_2, \theta_v, \sqrt{\sigma_{vb}^2 + \sigma_{vs}^2}, \sigma_{vb}) S(\phi, \phi_h, \sqrt{\sigma_{hb}^2 + \sigma_{hs}^2}, \sigma_{hb}) \quad (35)$$

The convolution with the surface feature function essentially broadens the edges of the angular response functions. The convolved expressions for the specular and diffuse terms are

$$\begin{aligned} \tilde{N}_{\text{spec}}(\hat{\theta}_1, \lambda, \theta_2, \phi) &= \int d\phi' \int d\theta'_2 N_{\text{spec}}(\hat{\theta}_1, \lambda, \theta_2 - \theta'_2, \phi) F_s(\theta'_2, \phi') = \\ N_0 \epsilon(\lambda) R(\sin \hat{\theta}_1, \lambda) P_{\text{spec}}(\sin \hat{\theta}_1, \lambda) \hat{E}_\theta(\theta_2 - 2\hat{\theta}_1) \hat{E}_\phi(\phi) \end{aligned} \quad (36)$$

$$\begin{aligned} \tilde{N}_{\text{diff}}(\hat{\theta}_1, \lambda, \theta_2, \phi) &= \int d\phi' \int d\theta'_2 N_{\text{diff}}(\hat{\theta}_1, \lambda, \theta_2 - \theta'_2, \phi) F_s(\theta'_2, \phi') = \\ N_0 \epsilon(\lambda) \frac{R(\sin \hat{\theta}_1, \lambda) (1 - P_{\text{spec}}(\sin \hat{\theta}_1, \lambda))}{J_0(\sin \hat{\theta}_1, \lambda)} \times \\ \int d\theta'_2 d\phi' J(\sin \hat{\theta}_1, \lambda, \sin(\theta'_2 - \hat{\theta}_1), \phi') \cos(\theta'_2 - \hat{\theta}_1) \hat{E}_\theta(\theta_2 - \theta'_2) \hat{E}_\phi(\phi - \phi') \end{aligned} \quad (37)$$

in which

$$\hat{E}_\theta(\theta_2) = S(\theta_2, \theta_v, \sqrt{\sigma_{vb}^2 + \sigma_{vs}^2}, \sigma_{vb}), \quad (38)$$

$$\hat{E}_\phi(\phi) = S(\phi, \phi_h, \sqrt{\sigma_{hb}^2 + \sigma_{hs}^2}, \sigma_{hb}) \quad (39)$$

C. Reflected grazing angle scans

To compare the angular scans in θ_2 with the scattering model, we set $\phi = 0$. Then we have, for the specular term,

$$\begin{aligned} & \tilde{N}_{\text{spec}}(\hat{\theta}_1, \lambda, \theta_2, 0) \\ &= N_0 \epsilon(\lambda) R(\sin \hat{\theta}_1, \lambda) P_{\text{spec}}(\sin \hat{\theta}_1, \lambda) \hat{E}_\theta(\theta_2 - 2\hat{\theta}_1) \hat{E}_\phi(0) \end{aligned} \quad (40)$$

For the diffuse term, since the angular variation in θ_2 is much larger than $\sqrt{\sigma_{vb}^2 + \sigma_{vs}^2}$, we can approximate the angular response function in θ_2 as a rectangular window times $\hat{E}_\theta(0)$, so that diffuse term becomes

$$\begin{aligned} \tilde{N}_{\text{diff}}(\hat{\theta}_1, \lambda, \theta_2, 0) &\approx N_0 \epsilon(\lambda) \frac{R(\sin \hat{\theta}_1, \lambda) (1 - P_{\text{spec}}(\sin \hat{\theta}_1, \lambda))}{J_0(\sin \hat{\theta}_1, \lambda)} \hat{E}_\theta(0) \times \\ &\int_{-\theta_v + \theta_2}^{\theta_v + \theta_2} d\theta'_2 \int d\phi' J(\sin \hat{\theta}_1, \lambda, \sin(\theta'_2 - \hat{\theta}_1), \phi') \cos(\theta'_2 - \hat{\theta}_1) \hat{E}_\phi(-\phi') \\ &\approx N_0 \epsilon(\lambda) \frac{R(\sin \hat{\theta}_1, \lambda) (1 - P_{\text{spec}}(\sin \hat{\theta}_1, \lambda))}{J_0(\sin \hat{\theta}_1, \lambda)} \hat{E}_\theta(0) \hat{E}_\phi(0) \times \\ &\int_{-\theta_v + \theta_2}^{\theta_v + \theta_2} d\theta'_2 \int_{-\pi}^{\pi} d\phi' J(\sin \hat{\theta}_1, \lambda, \sin(\theta'_2 - \hat{\theta}_1), \phi') \cos(\theta'_2 - \hat{\theta}_1) \end{aligned} \quad (41)$$

In the last step, we have used the fact that the angular variation of J in ϕ is typically much smaller than ϕ_h , so that the integral over the response function may be replaced by an integral over the full range in ϕ , times the value of the response function at $\phi = 0$.

Since the data is rescaled to its maximum value at the angle θ_2^{max} as given in Table VI, we compare the data with the rescaled ratio

$$r_\theta(\theta_2) = \frac{\tilde{N}(\hat{\theta}_1, \lambda, \theta_2, 0)}{\tilde{N}(\hat{\theta}_1, \lambda, \theta_2^{\text{max}}, 0)} = \frac{n_\theta(\hat{\theta}_1, \lambda, \theta_2)}{n_\theta(\hat{\theta}_1, \lambda, \theta_2^{\text{max}})} \quad (42)$$

in which

$$\begin{aligned} n_\theta(\hat{\theta}_1, \lambda, \theta_2) &= P_{\text{spec}}(\sin \hat{\theta}_1, \lambda) \hat{E}_\theta(\theta_2 - 2\hat{\theta}_1) + \frac{(1 - P_{\text{spec}}(\sin \hat{\theta}_1, \lambda))}{J_0(\sin \hat{\theta}_1, \lambda)} \hat{E}_\theta(0) \times \\ &\int_{-\theta_v + \theta_2}^{\theta_v + \theta_2} d\theta'_2 \int_{-\pi}^{\pi} d\phi' J(\sin \hat{\theta}_1, \lambda, \sin(\theta'_2 - \hat{\theta}_1), \phi') \cos(\theta'_2 - \hat{\theta}_1) \end{aligned} \quad (43)$$

D. Out-of-plane reflected angle scans

To compare the angular scans in ϕ with the scattering model, we note that for these scans, $\theta_2 = 2.6^\circ$, and $\theta_1 = 1.5^\circ$. Since

$$|\theta_2 - 2\hat{\theta}_1 \pm \theta_v| \gg \sqrt{\sigma_{vb}^2 + \sigma_{vs}^2},$$

the angular response function in θ_2 may be approximated by $\hat{E}_\theta(0)$. Then we have, for the specular term,

$$\begin{aligned} \tilde{N}_{\text{spec}}(\hat{\theta}_1, \lambda, \theta_2, \phi) \\ = N_0 \epsilon(\lambda) R(\sin \hat{\theta}_1, \lambda) P_{\text{spec}}(\sin \hat{\theta}_1, \lambda) \hat{E}_\theta(0) \hat{E}_\phi(\phi) \end{aligned} \quad (44)$$

For the diffuse term, as in the previous section, we can approximate the angular response function in θ_2 as a rectangular window. However, for the ϕ dependence, since the width of the diffuse scattering distribution in ϕ is comparable to σ_{hb} and σ_{hs} , we must keep the full form of the convolution integral:

$$\begin{aligned} \tilde{N}_{\text{diff}}(\hat{\theta}_1, \lambda, \theta_2, \phi) &\approx N_0 \epsilon(\lambda) \frac{R(\sin \hat{\theta}_1, \lambda) (1 - P_{\text{spec}}(\sin \hat{\theta}_1, \lambda))}{J_0(\sin \hat{\theta}_1, \lambda)} \hat{E}_\theta(0) \times \\ &\int_{-\theta_v + \theta_2}^{\theta_v + \theta_2} d\theta'_2 \int d\phi' J(\sin \hat{\theta}_1, \lambda, \sin(\theta'_2 - \hat{\theta}_1), \phi') \cos(\theta'_2 - \hat{\theta}_1) \hat{E}_\phi(\phi - \phi') \\ &\approx N_0 \epsilon(\lambda) \frac{R(\sin \hat{\theta}_1, \lambda) (1 - P_{\text{spec}}(\sin \hat{\theta}_1, \lambda))}{J_0(\sin \hat{\theta}_1, \lambda)} \hat{E}_\theta(0) \times \\ &2\theta_v \cos(\theta_2 - \hat{\theta}_1) \int d\phi' J(\sin \hat{\theta}_1, \lambda, \sin(\theta_2 - \hat{\theta}_1), \phi') \hat{E}_\phi(\phi - \phi') \end{aligned} \quad (45)$$

In the last line, we have approximated the integration over θ'_2 by neglecting the variation in $J(\sin \hat{\theta}_1, \lambda, \sin(\theta'_2 - \hat{\theta}_1), \phi') \cos(\theta'_2 - \hat{\theta}_1)$ with θ'_2 over the small angular range from $-\theta_v + \theta_2$ to $\theta_v + \theta_2$.

The convolution integral in ϕ may be done analytically, using the form of $J(\sin \hat{\theta}_1, \lambda, \sin(\theta'_2 - \hat{\theta}_1), \phi')$ given above, in the small angle approximation ($\phi \ll 1$). The analytic result (not given here) was used for comparison with the ϕ data scans shown in the following section.

Since the data is rescaled to its maximum value at the angle $\phi^{\text{max}} \approx 0$, we compare the data with the ratio

$$r_\phi(\phi) = \frac{\tilde{N}(\hat{\theta}_1, \lambda, \theta_2, \phi)}{\tilde{N}(\hat{\theta}_1, \lambda, \theta_2, \phi^{\text{max}})} = \frac{n_\phi(\hat{\theta}_1, \lambda, \theta_2, \phi)}{n_\phi(\hat{\theta}_1, \lambda, \theta_2, \phi^{\text{max}})} \quad (46)$$

in which

$$n_\phi(\hat{\theta}_1, \lambda, \theta_2, \phi) = P_{\text{spec}}(\sin \hat{\theta}_1, \lambda) \hat{E}_\phi(\phi) + \frac{2\theta_v(1 - P_{\text{spec}}(\sin \hat{\theta}_1, \lambda)) \cos(\theta_2 - \hat{\theta}_1)}{J_0(\sin \hat{\theta}_1, \lambda)} \int d\phi' J(\sin \hat{\theta}_1, \lambda, \sin(\theta_2 - \hat{\theta}_1), \phi') \hat{E}_\phi(\phi - \phi') \quad (47)$$

E. Global fits to the angular scattering data

The X-ray scattering measurements shown in Fig. 21 to Fig. 25 have been compared with the predictions of the theory described above. For the θ_2 scans, the comparisons were made to Eq. 42; for the ϕ scans, comparisons were made to Eq. 46. A simultaneous global fit to all the angular scans was done. Many of the parameters were fixed, based on the no-sample characterization of the beam and detector. The rms roughness, which is well determined by the AFM measurements, was also fixed. The free parameters in the fit were the roughness ratio $\tau = T/\sigma$, which is not precisely determined from the AFM measurements; the long-wavelength rms surface angular variation parameters σ_{vs} and σ_{hs} , which were not directly measured; and the parameters a , b and c , which allow for a systematic setting error in the angle of incidence. In addition, for each of the ϕ fits, an overall offset of the center of the model distribution from the $\phi = 0$ point was allowed as an additional free parameter.

A summary of all the model parameters is given in Table VIII, together with the standard errors from the fit for the fitted parameters. The fitted value of τ is smaller than the values (166 ± 76 , 213 ± 169) extracted from the AFM measurements for sample #1, but it is consistent with these measurements given their large errors. It should be noted that many of the parameters are strongly correlated: for example, σ may be reduced while σ_{vs} and σ_{hs} are increased, with little change in the quality of the overall fits.

In Fig. 26 to Fig. 30, we compare each angular scan with the model prediction. The specular and diffuse components of the scattering are shown separately. The light gray band indicates the 68% confidence level for the total model prediction. Inspection of the figures shows that, for the most part, the model does a reasonably good job of representing the measurements. The overall R^2 value for the global fit is 0.92.

Parameter	Value	Source
σ_{vb}	0.039°	Table 2
θ_v	0.837°	Table 2
σ_{hb}	0.162°	Table 3
ϕ_h	1.13°	Table 3
σ	95 nm	Table 1
τ	85.7 ± 1.3	Global fit
a	$-0.16 \pm 0.02^\circ$	Global fit
b	0.863 ± 0.008	Global fit
c	$0.005 \pm 0.0004/^\circ$	Global fit
σ_{vs}	$0.75 \pm 0.04^\circ$	Global fit
σ_{hs}	$0.35 \pm 0.03^\circ$	Global fit

TABLE VIII. Model parameter values used for global fit to the angular distribution data. For the fitted parameters, the standard errors from the fit are given. In addition, for each of the ϕ fits, an overall offset of the center of the model distribution from the $\phi = 0$ point was allowed as an additional free parameter. These offsets, which ranged from -0.01° to -0.11° , are not shown in the table.

F. Reflectivity measurements

1. Correction for detector geometric efficiency

The “observed reflectivity” data presented in Sec. IV C 1 should be compared with the smooth-surface reflectivity, computed from the LBNL database, multiplied by the geometric efficiency of the detector. With no sample in place, the detector at $\theta_2 = \phi = 0$ measures a photon number given by

$$N_{\text{det},0}(\lambda) = N_0\epsilon(\lambda). \quad (48)$$

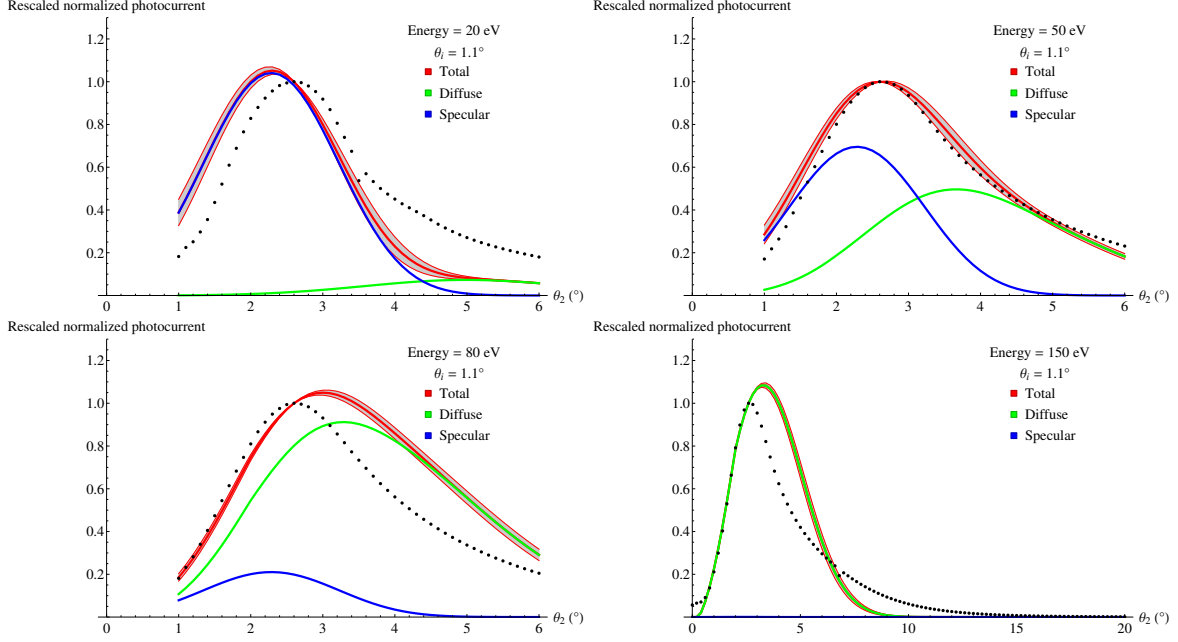


FIG. 26. Data sets Th1-Th4: Comparison between measurement and X-ray scattering model, θ_2 scans, for $\theta_1 = 1.5^\circ$ and various energies. The gray band represents the mean-prediction 95% confidence level associated with the fit.

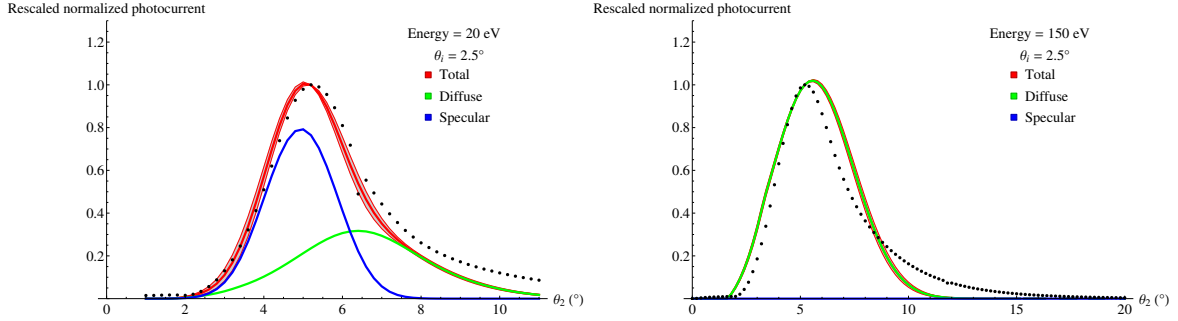


FIG. 27. Data sets Th5-Th6: Comparison between measurement and X-ray scattering model, θ_2 scans, for $\theta_1 = 3^\circ$ and various energies. The gray band represents the mean-prediction 95% confidence level associated with the fit.

With the sample in place, the detector at θ_2 and $\phi = 0$ measures $N_{\text{det}}(\hat{\theta}_1, \lambda, \theta_2, 0)$, given by Eq. 30. The “observed reflectivity” at θ_2 and $\phi = 0$ is

$$\begin{aligned}
 R_{\text{obs}}(\hat{\theta}_1, \lambda, \theta_2) &= \frac{N_{\text{det}}(\hat{\theta}_1, \lambda, \theta_2, 0)}{N_{\text{det},0}(\lambda)} \\
 &= \frac{N_{\text{spec}}(\hat{\theta}_1, \lambda, \theta_2, 0) + N_{\text{diff}}(\hat{\theta}_1, \lambda, \theta_2, 0)}{N_{\text{det},0}(\lambda)}
 \end{aligned} \tag{49}$$

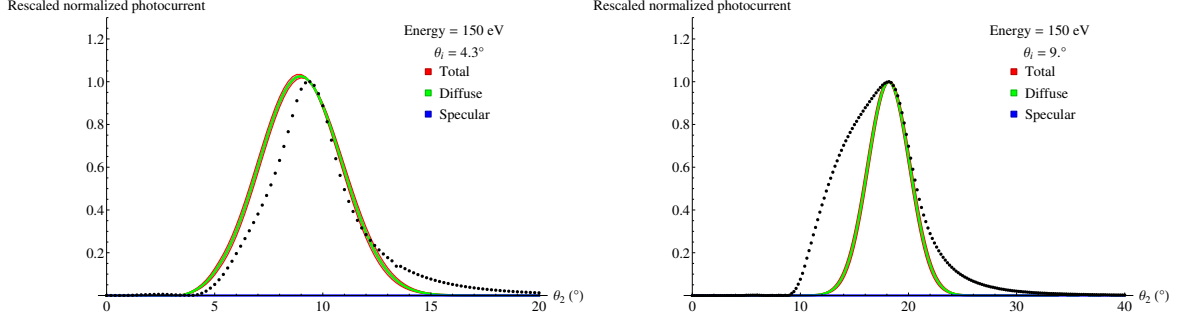


FIG. 28. Data sets Th7-Th8: Comparison between measurement and X-ray scattering model, θ_2 scans, for $\theta_1 = 5^\circ$ and $\theta_1 = 10^\circ$, and 150 eV. The gray band represents the mean-prediction 95% confidence level associated with the fit.

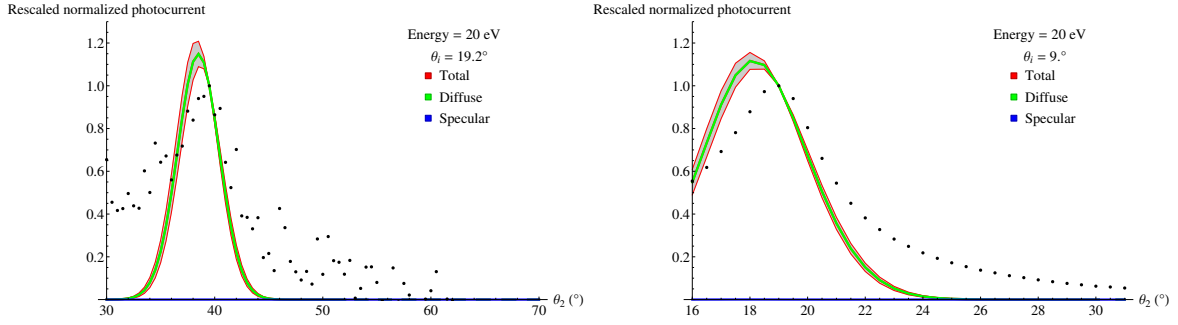


FIG. 29. Data sets Th9-Th10: Comparison between measurement and X-ray scattering model, θ_2 scans, for $\theta_1 = 10^\circ$ and $\theta_1 = 20^\circ$, and 20 eV. The gray band represents the mean-prediction 95% confidence level associated with the fit.

Using the previous expressions and the fact that $\hat{E}_\theta(0) \approx \hat{E}_\phi(0) \approx 1$ we find that the observed reflectivity is given by

$$R_{\text{obs}}(\hat{\theta}_1, \lambda, \theta_2) = R(\sin \hat{\theta}_1, \lambda) G_{\text{eff}}(\hat{\theta}_1, \lambda, \theta_2) \quad (50)$$

in which the geometric efficiency is

$$G_{\text{eff}}(\hat{\theta}_1, \lambda, \theta_2) = P_{\text{spec}}(\sin \hat{\theta}_1, \lambda) \hat{E}_\theta(\theta_2 - 2\hat{\theta}_1) + \frac{(1 - P_{\text{spec}}(\sin \hat{\theta}_1, \lambda))}{J_0(\sin \hat{\theta}_1, \lambda)} \int_{-\theta_v + \theta_2}^{\theta_v + \theta_2} d\theta'_2 \int_{-\pi}^{\pi} d\phi' J(\sin \hat{\theta}_1, \lambda, \sin(\theta'_2 - \hat{\theta}_1), \phi') \cos(\theta'_2 - \hat{\theta}_1) \quad (51)$$

The geometric efficiency has been computed for the incident and reflected angles associated with the data sets in Table IV, using the model parameters given in Sec. V E. The

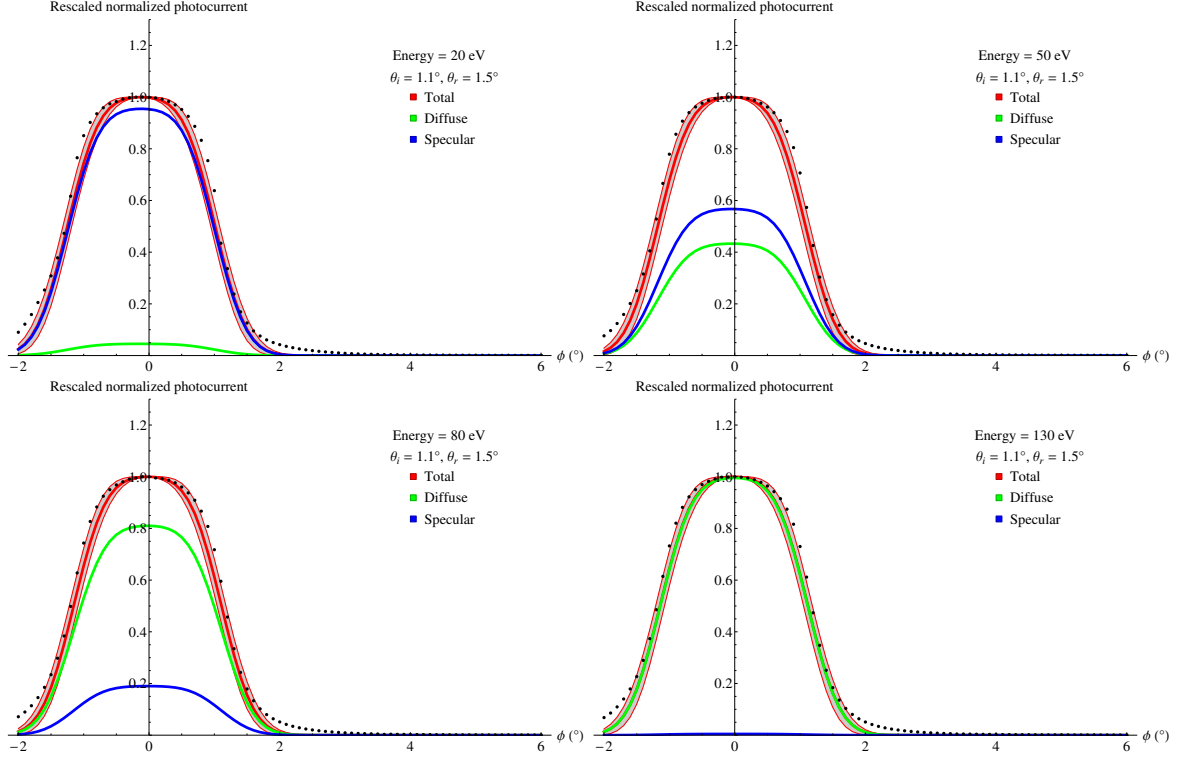


FIG. 30. Data sets Ph1-Ph4: Comparison between measurement and X-ray scattering model, ϕ scans, for $\theta_1 = 1.5^\circ$, $\theta_2 = 2.6^\circ$ and various energies. The gray band represents the mean-prediction 95% confidence level associated with the fit.

results are presented in Fig. 31. For most of the energy range, the geometric efficiency is on the order of 40%. It increases at very low energies, where the scattering is mostly specular and hence confined to a narrower angular range.

In Fig. 32, we compare the observed reflectivity from the X-ray data (Fig. 19, on a linear scale) with the expectation based on the smooth-surface reflectivity from the LBNL database multiplied by the computed geometric efficiency of the detector. As the figure shows, the X-ray data are a factor of at least 3 times lower than the expectation. As noted above, we attribute this reduction in reflectivity to long-wavelength surface features on the sample.

2. Effective reflectivity for sample #1, from a simulation of scattering from a grooved surface

Following the hypothesis discussed in Sec. IV C 3, we have done a simulation of specular scattering by ray-tracing (geometric optics) from a grooved surface, to estimate the effective reduction in reflectivity. A graphical illustration of the simulation is given in Fig. 33. This

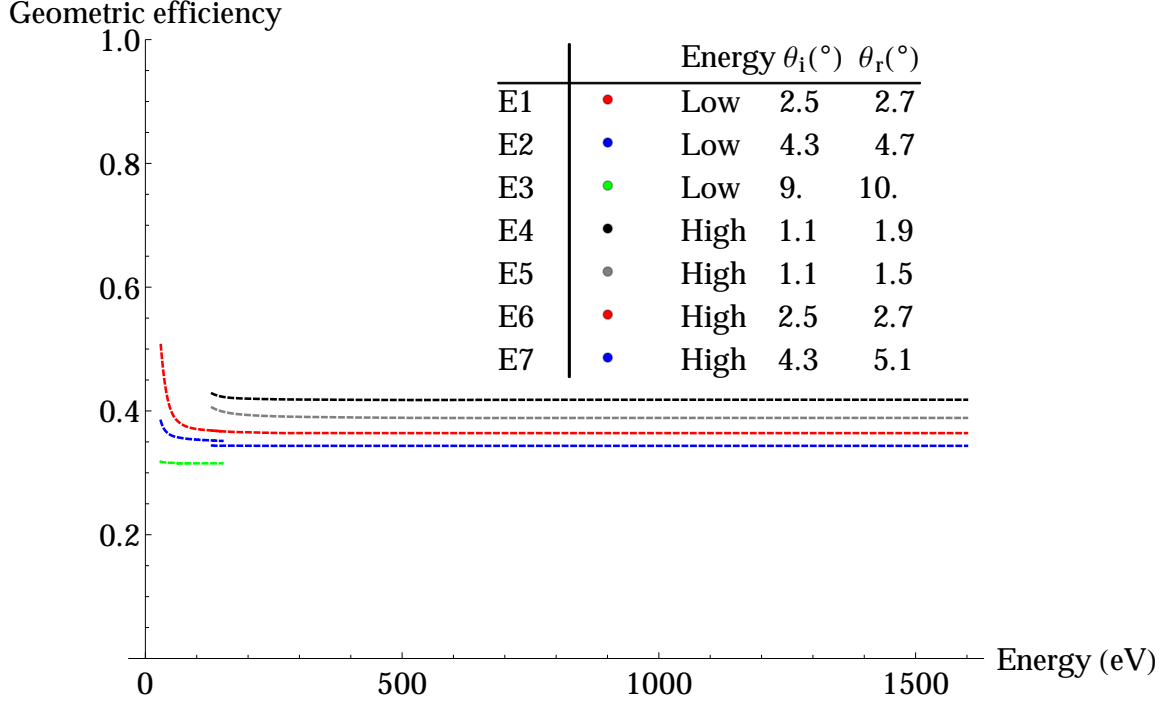


FIG. 31. Geometric efficiency, as a function of energy, for the data sets listed in Table IV.

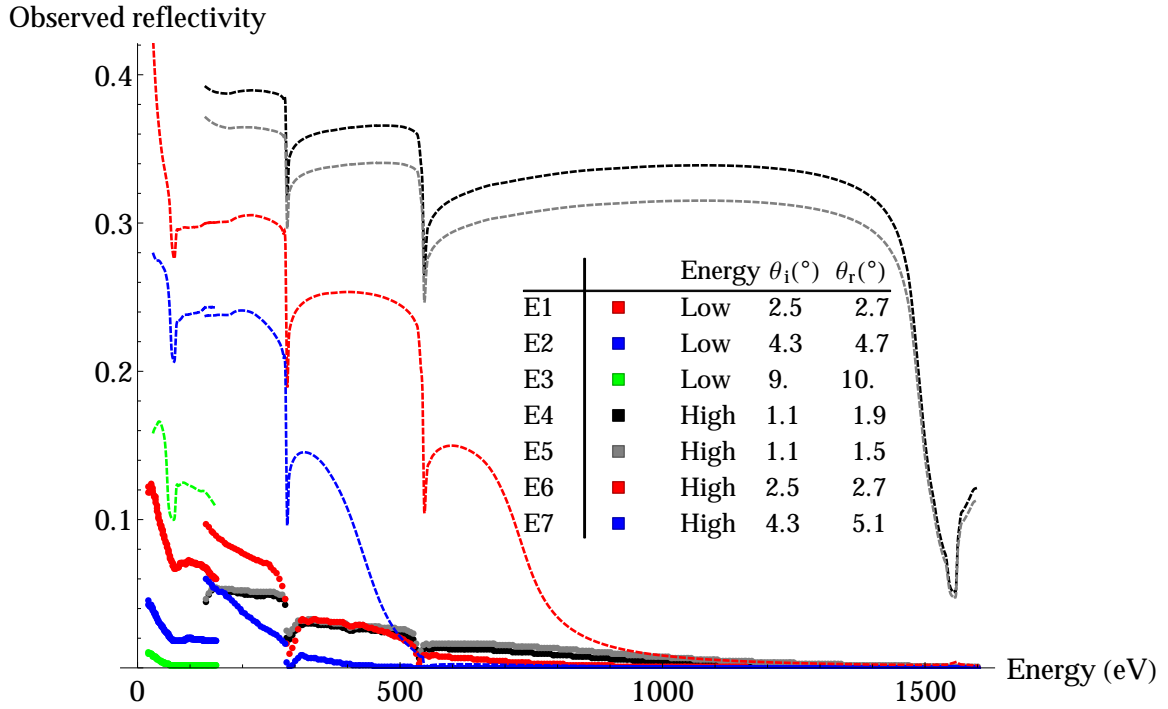


FIG. 32. Observed reflectivity, as a function of energy, aluminum sample #1, and comparison with scattering model (dashed lines)

figure corresponds to grooves which are perfectly aligned with the beam direction. The incident grazing angle is 3° . The distance units are arbitrary, since only the slope of the surface (ratio of depth to period) is important for determining the angular spread of the reflected rays. One can clearly see the scattered rays having a broad distribution in the out-of-plane angle, resulting from specular reflection from the sides of the grooves. The reduction in the observed reflectivity arises from the fact that, for a fixed angular location of the detector, the grooves scatter many rays away from the detector's direction. The groove depth-to-period ratio of about 0.5 was chosen by comparing the results of the simulation with the observed reflectivity from the X-ray data (see Fig. 35 below) and choosing a depth which gave approximate consistency with the data.

Fig. 9 indicates that, for sample #1, the period of the groove structure is of order $5\text{ }\mu\text{m}$. Then, $5\text{ }\mu\text{m}$ equals one unit of distance in Fig. 33. The groove depth is then about $2.5\text{ }\mu\text{m}$, similar to what is shown in Fig. 9.

Since it is likely that the actual grooves are not straight or perfectly aligned with the beam, in the simulation we have assumed a uniform random distribution in the angle of the grooves relative to the beam, with a width of $\pm 5^\circ$. In addition, for simplicity, only specular single scattering is considered.

In Fig. 34, two angular distributions from the simulation are shown. For the out-of-plane distribution, the events shown correspond to those falling in the detection window in reflected angle (i.e., equal to the angle of incidence $\pm 0.837^\circ$). Similarly, for the reflected angle distribution, the events shown correspond to those falling in the detection window in out-of-plane angle (i.e., equal to $\pm 1.13^\circ$).

These distributions represent roughly the rays entering the detector for purely specular reflection. As such, they may be compared with the spreads in specular component of the scattering obtained from the fits to the X-ray scattering angular distributions presented in Sec. V E. This comparison is shown in Table IX. For the out-of-plane angle, the results from the fits are comparable to the results from the simulation[7]. For the reflected angle, the simulation indicates a much smaller rms value than obtained from the fits. However, this is not so surprising, since the simulation assumes no variation in the surface in the direction parallel to the grooves (the x -direction). For a real surface, such as that shown in Fig. 9, there will also be some long-wavelength angular variation along the grooves, which will contribute to an increase in the rms width of the reflected angle distribution.

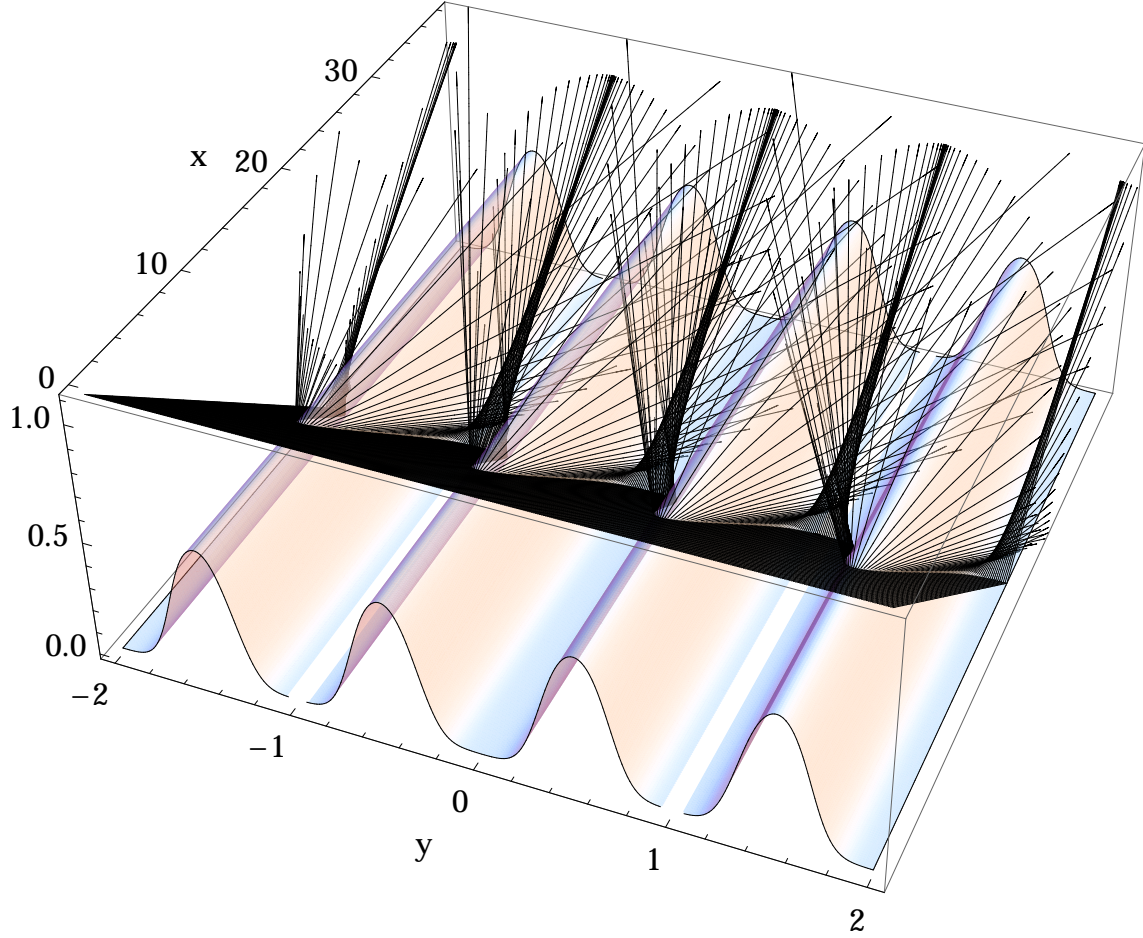


FIG. 33. Illustration of scattering from a grooved surface. For correspondence with the measured groove structure shown in Fig. 9, one distance unit corresponds to $5\ \mu\text{m}$. The rays are incident with a grazing angle of 3° , and the groove depth is about $2.5\ \mu\text{m}$.

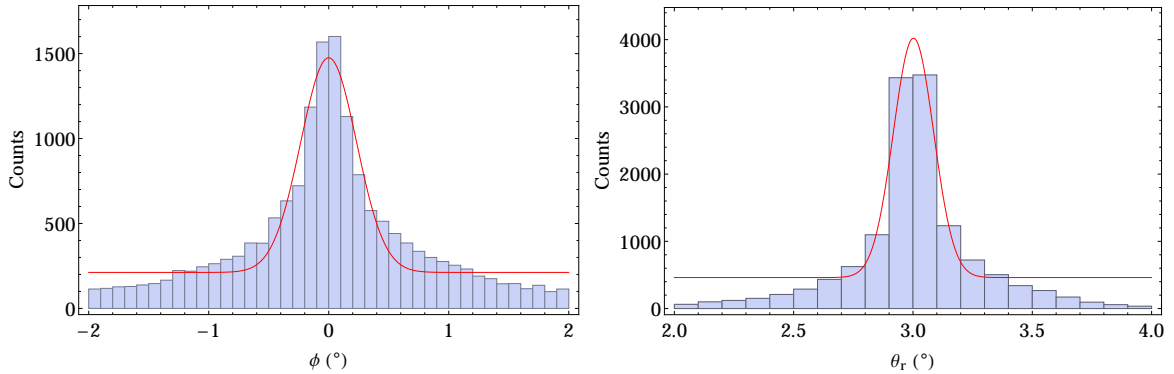


FIG. 34. Angular distributions for the simulation of groove scattering. The red curves are best-fit Gaussians with a flat background. Left: out-of-plane angle distribution; rms width of best-fit Gaussian: 0.23° . Right: in-plane reflected angle distribution; rms width of best-fit Gaussian: 0.08° .

Distribution	rms value	rms value
	from fits	from simulation
out-of-plane angle	0.35°	0.23°
in-plane reflected angle	0.75°	0.08°

TABLE IX. Comparisons between rms Gaussian widths of the specular component from fits to the angular distribution and from simulation

To estimate the observed reflectivity in the presence of the grooves, the effective reflectivity is computed by counting the number of photons scattered into the detector for a given reflected angle setting. This effective reflectivity is multiplied by the geometric efficiency of the detector, computed as described above in Sec. V F 1, which accounts for the additional loss of signal resulting from diffuse scattering, to obtain the observed reflectivity. In Fig. 35, the results for the observed reflectivity from the simulation are compared with the data. Given the inconsistencies in the data, and the crudeness of the groove scattering simulation, it is hard to make precise comparisons, but the hypothesis upon which the simulation is based does roughly account for the reduced reflectivity.

3. *Effective reflectivity for sample #2*

Sample #2 has a grooved surface similar to that of sample #1 (see Fig. 11) on the 10- μm -scale, but has a much lower reflectivity. The difference is most likely due to the additional pattern of ridges on the mm-scale, visible on the surface of sample #2 in Fig. 8. These features have a scale larger than that of the beam vertical height (rms $\sim 100\ \mu\text{m}$) and so would be expected to modify the effective reflectivity in a major way, which could depend in detail on the surface feature profile and the direction of the beam relative to it. Since we do not have detailed information on the surface feature profile at the mm-scale for sample #2, it is very difficult to make any prediction about the effective reflectivity.

VI. SUMMARY

In this paper, we have presented measurements of X-ray scattering from a technical aluminum vacuum chamber surface, whose surface features have been characterized by AFM

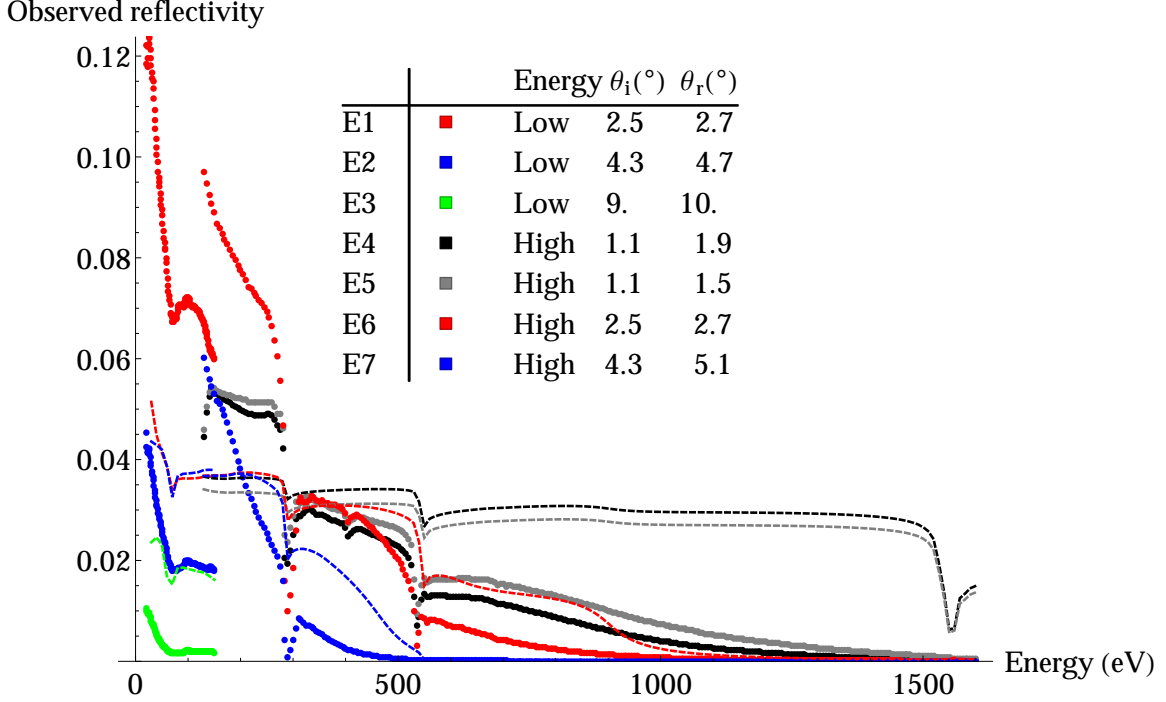


FIG. 35. Observed reflectivity, as a function of energy, aluminum sample #1, and comparison with scattering model including grooved surface scattering (dashed lines)

measurements. We have compared the measured angular distributions with the predictions of an analytical scattering model including both specular and diffuse scattering, based on scalar Kirchhoff theory [5, 6].

For surface parameters roughly in line with those measured via AFM, we find reasonable agreement between the theory and the measurements for the diffuse scattering distributions. To explain the angular distributions in the energy and angular range dominated by specular reflection, we must assume long-wavelength angular variations on the surface of order a few tenths of a degree. These angular variations may be related to surface features which were observed in the AFM measurements.

Absolute reflectivity measurements were also made. There are internal inconsistencies in these data; nevertheless, they indicate a much smaller reflectivity than would be expected based on smooth-surface reflectivity data from the LBNL database[4]. The explanation for this reduced reflectivity appears to be related to long-wavelength structures on the surface, which scatter photons out of the acceptance of the detector. For sample #1, ray tracing using a simple model of a grooved surface gives an estimated reduction in observed reflectivity

which is in semi-quantitative agreement with the data.

The model of specular and diffuse scattering from a stochastically rough vacuum chamber surface used in **Synrad3D** has been approximately validated by these experiments. However, the reflectivity data point out the additional importance of long-wavelength systematic surface variations on the scattering. For **Synrad3D** simulations of scattering from vacuum chambers with such long-wavelength features, the features should be incorporated into the geometry of the chamber surface model used in **Synrad3D**.

ACKNOWLEDGMENTS

We wish to acknowledge the support and help of Roberto Cimino (Istituto Nazionale di Fisica Nucleare), Sara Casalbuoni (Karlsruhe Institute of Technology) and Franz Schaefer (Helmholtz Zentrum Berlin) during the X-ray scattering measurements at BESSY II.

-
- [1] M. A. Palmer *et al.*, “The Conversion and Operation of the Cornell Electron Storage Ring as a Test Accelerator (CesrTA) for Damping Rings Research and Development’,” in *Proceedings of the 2009 Particle Accelerator Conference*, Vancouver, BC (2009), p. 4200–4204.
 - [2] G. Dugan & D. Sagan, “Synrad3D Photon Propagation and Scattering Simulation,” in *Proceedings of ECLOUD 2010: 49th ICFA Advanced Beam Dynamics Workshop on Electron Cloud Physics*, K. Smolenski, Ed., Ithaca, NY (in press), Paper PST08.
 - [3] G. Dugan & D. Sagan, “SYNRAD3D Photon Tracking Program,” Tech. rep., Cornell University (2012), <http://www.lepp.cornell.edu/~dcs16/synrad3d.pdf>.
 - [4] B. L. Henke, E. M. Gullikson & J. C. Davis, “X-Ray Interactions: Photoabsorption, Scattering, Transmission, and Reflection at $E = 50\text{--}30,000$ eV, $Z = 1\text{--}92$,” *At. Data Nucl. Data Tables* **54**, p. 181–342 (Jul. 1993).
 - [5] P. Beckmann & A. Spizzichino, *The Scattering of Electromagnetic Waves from Rough Surfaces*, Pergamon Press, New York (1963).
 - [6] J. A. Ogilvy, *Theory of Wave Scattering from Random Rough Surfaces*, Hilger, Bristol (1993).
 - [7] This particular surface composition has been chosen because, as discussed below, its absorption edges correspond to those observed in the reflectivity measurements presented here.

- [8] H. Hogrefe & C. Kunz, “Soft X-Ray Scattering from Rough Surfaces: Experimental and Theoretical Analysis,” *Appl. Opt.* **26**, p. 2851–2859 (Jul. 1987).
- [9] R. J. Noll & P. Glenn, “Mirror Surface Autocovariance Functions and their Associated Visible Scattering,” *Appl. Opt.* **21**, p. 1824–1838 (May 1982).
- [10] F. Schafers & I. Packe, “BESSY II Reflectometer,” http://www.helmholtz-berlin.de/pubbin/igama_output?modus=datei&did=292 (2011).
- [11] The simulation, however, suggest that a distribution with long tails, such as a Lorentzian, would be more appropriate than a Gaussian.